Post-earthquake relaxation evidence for laterally variable viscoelastic structure and water content in the southern California mantle

Fred F. Pollitz

U.S. Geological Survey, Menlo Park, CA, USA

F. F. Pollitz, U.S. Geological Survey, 345 Middlefield Rd., MS 977, Menlo Park, CA 94025

This article has been accepted for publication and undergone full peer review but has not been through the copyediting, typesetting, pagination and proofreading process, which may lead to differences between this version and the Version of Record. Please cite this article as doi: 10.1002/2014JB011603

Abstract.

I re-examine the lower crust and mantle relaxation following two large events in the Mojave Desert: the 1992 M7.3 Landers and 1999 M7.1 Hector Mine, California, earthquakes. Time series from continuous GPS sites out to 300 km from the ruptures are used to constrain models of postseismic relaxation. Crustal motions in the Mojave Desert region are elevated above background for several years following each event. To account for broadscale relaxation of the lower crust and mantle, the Burgers body model is employed, involving transient and steady-state viscosities. Joint afterslip / postseismic relaxation modeling of the GPS time series up to one decade following the Hector Mine earthquake reveals a significant rheological contrast between a northwest-trending 'southwest domain' (that envelopes the San Andreas fault system and western Mojave Desert) and an adjacent 'northeast domain' (that envelopes the Landers and Hector Mine rupture areas in the central Mojave Desert). The steady-state viscosity of the northeast-domain mantle asthenosphere is inferred to be $\sim$ 4 times greater than that of the southwest domain. This pattern is counter to that expected for regional heat flow, which is higher in the northeast domain, but it is explicable by means of a non-linear rheology that includes dependence on both strain rate and water concentration. I infer that the southwest-domain mantle has a relatively low steady-state viscosity because of its high strain rate and water content. The relatively low mantle water content of the northeast domain is interpreted to result from the continual extraction of water through igneous and volcanic activity over the past $\sim$ 20 Myr.

1. Introduction

Satellite-based observations of post-earthquake relaxation have provided valuable data that constrain postseismic deformation processes. In diverse tectonic regimes, observations made from months to years following a $M \gtrsim 7$ earthquake permit the inference of lower crust and mantle rheology [*Savage*, 1983; *Cohen*, 1999; *Bürgmann and Dresen*, 2008; *Thatcher and Pollitz*, 2008; *Hammond et al.*, 2009; *Wright et al.*, 2013]. In the context of linear, radially stratified viscoelastic rheologies, inference of viscosities in the ductile sub-lithosphere typically yield a 'strong' lower crust, of effective viscosity $\gtrsim 10^{20}$ Pa s and a 'weak' upper mantle of effective viscosity $\lesssim 10^{19}$ Pa s. This pattern is confirmed by values of effective viscosity estimated in the context of stress- and temperature-dependent rheologies [*Freed et al.*, 2012], and yield a picture in which the lower crust is essentially elastic and the mantle relaxes vigorously on a timescale of years to decades following an earthquake.

Estimation of depth-dependent viscosity would ideally be based on harnessing available post-earthquake crustal motion data at both near-field and far-field distances from the earthquake source. This allows sampling of relaxation both in the shallow mantle, where it is expected to be vigorous and affect mainly near-field sites (e.g. within about two elastic plate thicknesses of the source), and the deeper mantle, where the relaxation is expected to be more subdued but also broader [e.g. *Cohen*, 1982; *Freed and Bürgmann*, 2004; *Hetland and Hager*, 2005; *Hearn et al.*, 2009] and affect mainly far-field sites. Using data at near-field distances is complicated by the possibilities of poro-elastic rebound [e.g. *Peltzer et al.*, 1996, 1998; *Fialko*, 2004] and shallow or deep afterslip [e.g. *Savage and Svarc*, 1997;

Perfettini and Avouac, 2007]. The former is considered most important very close to the fault zone based on clear distortions of very near-field postseismic motions constrained by InSAR [*Peltzer et al.*, 1996; *Jónsson et al.*, 2003]. Discrimination of broadscale lower crust and mantle relaxation is more challenging and has been based of two chief types of discriminants: 1. The vertical postseismic surface motions, for which the broadscale relaxation and shallow afterslip processes are predicted to be nearly anti-correlated, and 2. The far-field horizontal surface motions, which are negligible for afterslip and substantial for broadscale relaxation. Both types of discriminant have been used in practice [e.g. *Pollitz et al.*, 2000, 2001; *Nishimura and Thatcher*, 2003; *Pollitz*, 2003; *Freed and Bürgmann*, 2004; *Gourmelen and Amelung*, 2005; *Freed et al.*, 2007; *Pollitz and Thatcher*, 2010; *Freed et al.*, 2012].

In this study I use more than one decade of GPS observations of postseismic relaxation in the Mojave Desert, California, following the June 28, 1992 M7.3 Landers earthquake and October 16, 1999 M7.1 Hector Mine earthquake. These quakes occurred within the Eastern California Shear Zone (ECSZ) south of the Garlock fault, a zone of active deformation east of the San Andreas fault system. I apply models of quasi-static deformation to the postseismic relaxation following the Landers and Hector Mine quakes in order to infer radially and laterally variable viscoelastic structure. The most conservative approach towards inferring regional mantle viscoelastic structure is to restrict attention to far-field data in order to avoid complications of shallow afterslip and lower crust relaxation [e.g. *Freed et al.*, 2007, 2012]. The alternative is to include all available relaxation data but to consider simultaneously afterslip and lower crust and mantle relaxation, as has been done to interpret post-earthquake motions elsewhere [e.g. *Hearn et al.*, 2009; *Shao et al.*,

2011; *Rousset et al.*, 2012; *Huang et al.*, 2014; *Hu et al.*, 2014]. Given the benefits in terms of resolving regional viscoelastic structure [*Pollitz and Thatcher*, 2010; *Hines and Hetland*, 2013] and exploiting the relaxation signal that is expected to be vigorous in the near-field, I adopt the latter approach. Use of a wide aperture of observations carries the additional benefit that one may potentially constrain lateral variations in regional viscoelastic structure. Such variations have been deemed important in both theoretical studies [e.g. *Cohen*, 1994, 2000] and applied studies in strike-slip settings [*Ryder et al.*, 2011; *Pollitz et al.*, 2012; *Huang et al.*, 2014] and subduction zone settings [*Khazaradze et al.*, 2002; *Hu and Wang*, 2012; *Hu et al.*, 2014]. I will document that the post-Hector Mine GPS observations illuminate a first order contrast in rheological properties between the central Mojave Desert and the San Andreas plate boundary zone.

2. Data set

I utilize three-dimensional time series of 109 regional GPS sites within 300 km of the Hector Mine centroid (Figure 1). These are extracted from the Nevada Geodetic Laboratory (NGL) archive (http://geodesy.unr.edu/gps_timeseries/tenv3/NA12/). These time series have been processed by NGL in a fixed North America reference frame [*Blewitt et al.*, 2013]. I consider postseismic crustal deformation for the period between the 1992 Landers and 1999 Hector Mine earthquakes and in the 10.46 years following the 1999 Hector Mine earthquake, i.e., up to the time of the April 4, 2010 M7.2 El Mayor - Cucapah earthquake. Observed time series at selected sites are shown in Figure 2.

I seek to isolate the transient signal in the observed time series. This is the observed deformation that is not attributable to either steady background motions or seasonal signals. I assume a trial model consisting of time-dependent displacement produced by

afterslip $u_{\rm aft}(t)$ and broadscale relaxation $u_{\rm rel}$ and estimate: (1) a steady background velocity, (2) seasonal terms of the time series, and (3) (for those time series beginning before the 1999 Hector Mine earthquake) the coseismic displacement step of the Hector Mine earthquake. I then correct each observed time series for the background velocity and seasonal terms. Specifically, defining t_0 as the origin time of the 1999 Hector Mine earthquake, I parameterize a model postseismic time series displacement $u_{\rm mod}(t)$ as

$$u_{\rm mod}(t) = u_{\rm aft}(t) + u_{\rm rel}(t) + a_1 H(t-t_0) + a_2 + a_3(t-t_0)$$
$$+a_4\cos(2\pi t) + a_5\sin(2\pi t) + a_6\cos(4\pi t) + a_7\sin(4\pi t). \quad (1)$$

The a_1 term represents the coseismic jump in displacement at t_0, the a_2 term an initial displacement, the a_3 term the background (i.e., pre-1992 Landers) velocity, and remaining terms the annual and semi-annual seasonal displacements. Linear least squares inversion is used to minimize the L_2 norm of the difference $u_{\rm mod} - u_{\rm obs}$ and determine the seven constants a_j from observations $u_{\rm obs}(t)$ at distinct times $t = t_i$; typically hundreds or thousands of time samples are used in such an inversion. For the vertical time series, I assume that the background velocity is zero, hence the a_3 term is fixed at zero when fitting these time series. The corrected observed time series is then

$$u'_{\rm obs}(t) = u_{\rm obs}(t) - [a_2 + a_3(t-t_0) + a_4\cos(2\pi t) + a_5\sin(2\pi t) + a_6\cos(4\pi t) + a_7\sin(4\pi t)] \quad (2)$$

Observed corrected time series $u'_{\rm obs}$ at selected sites are shown in Figure 2. If no transient velocity signals were present, the time series in pre- and post-Hector Mine time intervals would be flat. The corrected time series generally exhibit a significant slope averaged over several years, particularly in the post-Hector Mine epoch, and several time series exhibit

curvature suggestive of a relaxation process with an exponentially decaying temporal dependence. Excursions in several time series during 2005, particularly in the vertical component, are attributable to the effects of the very wet winter of 2004-2005 [*Ji and Herring*, 2012].

I determine the average velocity following the Hector Mine event within distinct time intervals. Since the observed time series have considerable scatter, I first smooth all observed time series with parametric curves. Often, this curve is chosen to be a logarithmic function [e.g. *Freed et al.*, 2007, 2012], or a combination of a logarithmic function and a decaying exponential, which is more appropriate for prolonged (several years) periods of postseismic relaxation. As an alternative, here I use bi-cubic spline fitting of these time series. This involves a greater number of parameters but can better account for systematic trends in the time series. Corrected observations $u'_{\rm obs}(t_i)$ over the entire available time interval following the Hector Mine event are fit with a model of two separate cubic polynomials joined at break point $t_{\rm break}$:

$$u_{\rm cube}(t) = b_0 + b_1(t - t_{\rm break}) + b_2(t - t_{\rm break})^2 + b_3(t - t_{\rm break})^3 \quad (t < t_{\rm break})$$

$$u_{\rm cube}(t) = b_0 + b_1(t - t_{\rm break}) + b_4(t - t_{\rm break})^2 + b_5(t - t_{\rm break})^3 \quad (t \geq t_{\rm break}) \qquad (3)$$

This parameterization enforces the condition of continuity of displacement and velocity at $t = t_{\rm break}$, this reduces the number of parameters needed for the two cubic polynomials from 8 to 6. For a given time series the constants $\{b_j, j = 0, \cdots, 5\}$ are found by minimizing the misfit function

$$\chi^2 = \sum_{\substack{i \\ t_i > t_0}} \left(\frac{u'_{\rm obs}(t_i) - u_{\rm cube}(t_i)}{\sigma_i} \right)^2 \qquad (4)$$

where σ_i is the standard error in the observation. The estimated average observed velocity over any post-Hector Mine time interval (x_1, x_2) is

$$v_{\text{obs}} = \frac{u_{\text{cube}}(x_2) - u_{\text{cube}}(x_1)}{x_2 - x_1} \tag{5}$$

with standard error denoted by $\sigma_v(x_1, x_2)$, derived through propagation of errors through the cubic model fit of the data. Robust fits to the time series are generally obtained by choosing t_{break} to be two years after the Hector Mine event, i.e., $t_0 + 2$ years. This choice allows the bi-cubic polynomial parameterization to replicate accurately both logarithmic functions and a superposition of exponentially-decaying functions that may include one associated with a rapid transient (i.e., a decay time much shorter than two years). Note that the bi-cubic polynomial fits to the observed time series (green curves in Figure 2) accurately capture the smoothly varying trends in the data, even if these trends are not always consistent with the supposition of a monotonically decaying transient, e.g., the DSSC vertical or CSN1 north-component time series. This is what the bi-cubic curves are designed to do in order to stabilize the estimation of velocity by means of eqn 5.

The corrected observed horizontal velocity fields for three selected postseismic time periods are shown in Figure 3, and the vertical velocity fields in Figures 4, Figure S-1, and Figure S-2. The vertical velocity field is retained only at sites within 150 km of the Hector Mine rupture, as these are expected to exhibit the largest tectonic signals associated with excitation from the Hector Mine source. Since the background velocity field has, in principle, been subtracted, these velocity fields represent the transient velocity field that is attributable to processes unique to the postseismic epoch, e.g. afterslip and/or broadscale relaxation. The horizontal and vertical velocity fields conform closely to the quadrant pattern expected for these processes, suggesting that most of the background

velocity field has been subtracted from the initial observed velocity field. The vertical velocity pattern is a useful discriminant between the afterslip and deep (mantle) relaxation processes, and the pattern in Figures S-1 and 4 are anti-correlated with the coseismic vertical displacement field and therefore qualitatively consistent with deep relaxation rather than afterslip [*Pollitz et al.*, 2000, 2001].

Velocities are potentially contaminated by non-tectonic perturbations, the largest of which is likely that induced by the wet 2004-2005 winter, which affects many GPS time series (Figure 2). I find that the year 2005 excursions have a negligible effect on estimated velocities during the 2.5 - 10.46 years time period; these velocities are nearly unchanged if the 2005 portion of the time series are removed.

3. Models

3.1. Coseismic slip models

For the 1999 Hector Mine earthquake I use a 24-plane representation of the distributed slip model of *Jónsson et al.* [2002], which is based on joint GPS and InSAR dislocation modeling (Figure S-3). The slip distribution involves right-lateral slip up to about 6 meters on a $\sim$ 56 km length of faults that includes the Lavic Lake fault and a more northerly-trending branch that bifurcates from this fault (green traces in Figure 1).

A 7-plane approximation to the rupture model of *Wald and Heaton* [1994] is employed for the 1992 Landers earthquake. The event involved right-lateral slip up to about 7 meters over a length of $\sim$ 80 km.

3.2. Afterslip following the 1999 Hector Mine earthquake

I allow for possible afterslip using the *Jónsson et al.* [2002] slip surface and its downdip extension. The afterslip is parameterized with uniform right-lateral slip on each of $N_{\rm patch} = 32$ patches which envelop the *Jónsson et al.* [2002] Hector Mine coseismic rupture plane and continue on a down dip extension to 30 km depth. The vast majority of aftershocks lie north of $\sim 34.6°$N [*Li et al.*, 2002], i.e., within the northern area spanned by the assumed coseismic rupture plane and its down dip extension, but possible afterslip south of the aftershock region is included.

Afterslip is implemented kinematically and is not coupled with the viscoelastic flow. This is an alternative to a mechanically-driven afterslip process [e.g. *Perfettini and Avouac*, 2007] that would depend on the stress changes induced by the coseismic slip model. Here afterslip is realized with a Monte Carlo simulation of forward models. In one realization, the average afterslip $\bar{s}$ is randomized according to the uniform distribution: $\bar{s} = U(0, s_{\rm max})$, where $s_{\rm max}$ is a maximum average which I take to be 2.5 m. The slip values s_i on each of the afterslip patches are then randomized to $u_i = U(0, 1)$ and normalized to $\bar{s}$, i.e.

$$s_i = \bar{s} N_{\rm patch} \frac{u_i}{\sum_{i=1}^{N_{\rm patch}} u_i} \tag{6}$$

For a given afterslip model $\{s_i\}$, time-dependent deformation following the 1999 Hector Mine event is calculated by convolving this model with the static Green's functions on a spherically layered earth model and assuming an exponential time dependence:

$$u_{\rm aft}(\mathbf{r}, t) = \sum_i \int_{\mathbf{r}' \in {\rm patch}\, i} s_i \, G(\mathbf{r}, \mathbf{r}'; \hat{\mathbf{M}}_i) \, \left[1 \, - \, \exp\left(-\frac{t - t_0}{\tau_a} \right) \right] \qquad (t > t_0) \tag{7}$$

where $G(\mathbf{r}, \mathbf{r}'; \hat{\mathbf{M}}_i)$ is the static Green's function for a unit displacement component at $\mathbf{r}$ from a point source at $\mathbf{r}'$ with a given dislocation geometry on patch i, denoted by the

unit moment tensor $\hat{\mathbf{M}}_i$. The exponential time dependence is consistent with models of the afterslip process in a variety of tectonic settings. The time constant τ_a ranges from a few days to months for many studied earthquakes [e.g. *Shen et al.*, 1994; *Savage and Svarc*, 2005; *Perfettini and Avouac*, 2007]. I use the value $\tau_a = 0.25$ year, close to the value 0.32 ± 0.18 year obtained for near-field post-Hector Mine deformation [*Savage et al.*, 2003].

3.3. Lower crust and mantle relaxation

Viscoelastic relaxation of the lower crust and upper mantle is calculated using the spectral element method code VISCO2.5D, which yields a 3D quasi-static displacement field for 2D structures in a spherical geometry [*Pollitz*, 2014]. This approach assumes linear viscoelasticity and that the viscoelastic structure is azimuthally symmetric about a prescribed pole. Quasi-static displacements are first calculated in the Laplace transform domain, and time-domain displacement is then obtained through an inverse Laplace transform evaluation.

I choose the pole of symmetry to be at $-32.8°$N, $174.3°$E and define the model domain to be an annulus on the unit sphere between small circles located $90°$ and $98.63°$ from this pole (Figure 1c). This envelopes much of southern California from its southern coast region to adjacent Nevada and Arizona. The radial part of the domain extends from a depth of 300 km to earth's surface, hence the computational domain is of dimensions 8.63 geocentric degrees (960 km) $\times$300 km. A zero-displacement boundary condition is applied at the base of the model, and Robin boundary conditions meant to approximate the far-field decay of quasi-static displacements with lateral distance from the source is

applied to the annular boundaries. A sum over a series of azimuthal order numbers is used to synthesize the 3D quasi-static displacement field over the model volume.

This method is applied to the coseismic slip models of the Landers and Hector Mine earthquakes (section 3.1) to calculate post-earthquake relaxation in a defined volume around these sources, including regional GPS sites. Summing the contributions from both sources yields time series displacement from viscoelastic relaxation $u_{\mathrm{rel}}(t)$ at every point in the model volume.

3.4. Velocity

For given models of afterslip $u_{\mathrm{aft}}(t)$ and relaxation $u_{\mathrm{rel}}(t)$, model displacement $u_{\mathrm{mod}}(t)$ is given by eqn 1. To render the model directly comparable with the observed transient u'_{obs} that has the background and seasonal components removed, we consider that part of the model representing transient tectonic deformation:

$$u'_{\mathrm{mod}}(t) = u_{\mathrm{mod}}(t) - [a_1 + a_3(t-t_0) + a_4\cos(2\pi t) + a_5\sin(2\pi t) + a_6\cos(4\pi t) + a_7\sin(4\pi t)]$$

$$= u_{\mathrm{aft}}(t) + u_{\mathrm{rel}}(t) + a_1 H(t-t_0) \tag{8}$$

The coseismic step $a_1 H(t-t_0)$ is retained in $u'_{\mathrm{mod}}(t)$ (and implicitly in u'_{obs}) in order to help visualize the difference between pre-Hector Mine and post-Hector Mine transient displacement and to emphasize the size of these transients relative to the coseismic step.

The transient model velocity in a time interval (x_1, x_2) (that excludes the origin time t_0) is determined directly from u_{mod} as

$$v_{\mathrm{mod}} = \frac{u'_{\mathrm{mod}}(x_2) - u'_{\mathrm{mod}}(x_1)}{x_2 - x_1}. \tag{9}$$

4. Rheology models

4.1. Choice of rheology

In the Mojave Desert [*Pollitz*, 2003; *Freed et al.*, 2012] and elsewhere [e.g. *Pollitz*, 2005; *Hetland and Hager*, 2005, 2006; *Hearn et al.*, 2009; *Ryder et al.*, 2011; *Pollitz et al.*, 2012; *Wang et al.*, 2012; *Huang et al.*, 2014] it has been recognized that a transient rheology is necessary to explain the time-dependence of observed relaxation. An initial rapid transient and subsequent transition to more steady postseismic motions at much slower rates are consistent with laboratory observations of transient creep followed by steady state creep at much lower strain rates [*Chopra*, 1997; *Post*, 1977]. This behavior is often represented with a Burgers body, which may be represented with springs and dashpots as a Kelvin element in series with a Maxwell element (inset of Figure 5) associated with a transient viscosity and steady-state viscosity, respectively. The Maxwell component may be implemented as either a linear (stress-independent) rheology [e.g. *Pollitz*, 2003; *Hetland and Hager*, 2005] or non-linear (stress-dependent) rheology [*Freed et al.*, 2012]. I adopt the Burgers body model for the mantle with a linear rheology for its steady-state component, noting that its steady-state component can be reconciled with a stress-dependent rheology provided that the background stress is much larger than the stress change imparted by the imposed source. If that is the case, then a stress-dependent rheological law given by an Arrhenius relation [*Bürgmann and Dresen*, 2008] may be approximated by a stress-independent law for an equivalent (linear) Maxwell body with a stress-independent effective viscosity. This steady-state rheology may then be appended with a transient component using the Burgers body model. I assume a Maxwell rheology for the lower crust because its material relaxation time is typically several decades [*Thatcher and Pollitz*,

2008], an order of magnitude greater than the material relaxation time associated with the steady-state mantle viscosity, so a possible transient component cannot be resolved with the present data set.

I consider several viscoelastic models to characterize the regional postseismic deformation. All models have a Burgers body rheology in the upper mantle and Maxwell rheology in the lower crust. The Burgers body rheology [*Pollitz*, 2003; *Hetland and Hager*, 2005; *Hearn et al.*, 2009; *Segall*, 2010] is prescribed by bulk modulus κ, transient viscosity and shear modulus η_2 and μ_2, and steady state viscosity and shear modulus η_1 and μ_1. The Maxwell rheology is realized as an endmember alternatively by specifying $\eta_2 = \infty$ or the combination of $\eta_1 = \infty$ and $\mu_2 = 0$.

4.2. Laterally homogeneous models

A set of laterally homogeneous (i.e., radially stratified) models is represented in Figure 5. These models involve a mantle characterized by a Burgers body, a Maxwellian lower crust, and an elastic upper crust. The steady state viscosity in the mantle is assumed constant in the separate depth ranges 30 - 43 km and 43 - 220 km. The discontinuity at 43 km is meant to mark the base of a high-viscosity mantle lithosphere. This boundary is in reality not sharp and in the study area may be located somewhat deeper at > 50 km depth [*Lekic et al.*, 2011; *Smith-Konter et al.*, 2014]. The material between 220 and 300 km depth is assigned a Maxwell rheology with viscosity $\eta_1 = 10^{20}$ Pa s in order to account for the expected increase of viscosity with increasing pressure [e.g. *Karato and Jung*, 2003]. The ratio of steady state viscosity in the 30 - 43 km range to that in the 43 - 220 km range is assumed to equal 5, in conformity with laboratory-derived flow laws applied to typical uppermost mantle conditions [e.g. *Bürgmann and Dresen*, 2008; *Ranalli*,

1995]. Similarly, the ratio of lower crust to uppermost mantle viscosity is consistent with laboratory-derived flow laws for felsic or magic granulite [*Wilks and Carter*, 1990]. Models 1 to 5 are trial models that explore a range of steady-state and transient mantle viscosities. Model 6 is the preferred model of *Pollitz* [2003] based on three years of postseismic GPS observations. It represents a low-viscosity endmember of the considered models.

4.3. Laterally heterogeneous models

The physical state of the southern California crust and mantle are constrained by seismic velocity imaging [e.g. *Tian et al.*, 2007; *Yang et al.*, 2008; *Tape et al.*, 2010; *Schmandt and Humphreys*, 2010], the crustal thickness pattern [*Richards-Dinger and Shearer*, 1997; *Kohler and Davis*, 1997; *Zhu and Kanamori*, 2000; *Yan and Clayton*, 2007; *Ozakin and Ben-Zion*, 2014], and regional heat flow. Uppermost mantle seismic velocities exhibit an approximately northwest-southeast trending fabric with a contrast across a NW-SE trending boundary that roughly divides the western and central Mojave Desert [*Yang et al.*, 2008; *Schmandt and Humphreys*, 2010]. Heat flow values in southern California (Figure 6a) exhibit a step-like increase across a similar boundary dividing the western and central Mojave Desert, best seen when averaged in the N40°W direction (Figure 6b). The crustal thickness pattern determined by the above studies exhibit an approximate step in thickness from $\sim 28-30$ to ~ 33 km across roughly the same boundary. This is exemplified by the *Yan and Clayton* [2007] crustal thickness pattern in Figure S-4 based on teleseismic receiver function analysis, which is similar to the pattern obtained by the other studies.

I assume that the lateral variations in uppermost mantle seismic velocity, heat flow, and crustal thickness are diagnostic of different mantle rheologies in two contrasting domains

without regard to the precise nature of the origin of this difference. I construct a 2D viscoelastic structure consisting of separate 'northeast' and 'southwest' domains, the two domains being divided by a boundary that approximately coincides with the Lenwood-Lockhart fault and the southern San Andreas fault south of the Pinto Mountain fault (Figure 1). Trial viscoelastic structures are assumed laterally homogeneous within each respective domain.

In the next session I present evidence that these two domains possess very different viscoelastic structures. The crustal thickness, although possible to include as an independent parameter, is assigned the value 30 km under both domains. It is of secondary importance because the viscosities of the lower crust and mantle lithosphere are relatively large in all considered models, and thus these volumes accommodate little relaxation. The chief property affecting the postseismic relaxation will prove to be the transient and steady-state viscosities of the mantle asthenosphere.

5. Fit of rheology models to observed postseismic relaxation

5.1. Measures of model misfit

3D velocities in selected time periods are used to evaluate how well candidate rheology models fit the observed postseismic deformation field. Specifically, a number of non-overlapping time periods (x_1^j, x_2^j) are used to evaluate misfit separately for horizontal and vertical velocity components:

$$\chi^2_{\mathrm{H}}(x_1^j, x_2^j) = \sum_n \frac{\left[(v_E)^{jn}_{\mathrm{obs}} - (v_E)^{jn}_{\mathrm{mod}}\right]^2}{\left[\sigma^n_{v_E}(x_1^j, x_2^j)\right]^2} + \frac{\left[(v_N)^{jn}_{\mathrm{obs}} - (v_N)^{jn}_{\mathrm{mod}}\right]^2}{\left[\sigma^n_{v_N}(x_1^j, x_2^j)\right]^2} \quad (j = 1, 2, 3) \qquad (10)$$

$$\chi^2_{\mathrm{U}}(x_1^j, x_2^j) = \sum_n \frac{\left[(v_U)^{jn}_{\mathrm{obs}} - (v_U)^{jn}_{\mathrm{mod}}\right]^2}{\left[\sigma^n_{v_U}(x_1^j, x_2^j)\right]^2} \quad (j = 1, 2, 3) \qquad (11)$$

where $v^{jn}_{\rm obs}$ and $v^{jn}_{\rm mod}j$ are the observed and model velocity at site n in time interval j, respectively, and E, N, and U denote East, North, and Up components, respectively.

A related measure is the root-mean-square velocity misfit:

$$\mathrm{RMS\,v_H}(x_1^j, x_2^j) = \left(\frac{\chi^2_{\rm H}(x_1^j, x_2^j)}{\sum_n \frac{1}{\left[\sigma^n_{v_E}(x_1^j, x_2^j)\right]^2} + \frac{1}{\left[\sigma^n_{v_N}(x_1^j, x_2^j)\right]^2}} \right)^{\frac{1}{2}} \qquad (j = 1, 2, 3) \tag{12}$$

$$\mathrm{RMS\,v_U}(x_1^j, x_2^j) = \left(\frac{\chi^2_{\rm U}(x_1^j, x_2^j)}{\sum_n \frac{1}{\left[\sigma^n_{v_U}(x_1^j, x_2^j)\right]^2}} \right)^{\frac{1}{2}} \qquad (j = 1, 2, 3) \tag{13}$$

A final measure is the root-mean-square velocity misfit averaged over all time periods and over horizontal and vertical components:

$$\mathrm{RMS\,v} = \left(\frac{\sum_j \chi^2_{\rm H}(x_1^j, x_2^j) + \chi^2_{\rm U}(x_1^j, x_2^j)}{\sum_j \sum_n \frac{1}{\left[\sigma^n_{v_E}(x_1^j, x_2^j)\right]^2} + \frac{1}{\left[\sigma^n_{v_N}(x_1^j, x_2^j)\right]^2} + \frac{1}{\left[\sigma^n_{v_U}(x_1^j, x_2^j)\right]^2}} \right)^{\frac{1}{2}} \tag{14}$$

5.2. Laterally homogeneous models

Time-dependent variations in the post-earthquake relaxation are captured by considering average crustal velocity within the following three time intervals: $(x_1^1, x_2^1) = (0, 6\,\text{months}$, $(x_1^2, x_2^2) = (6\,\text{months}, 2.5\,\text{years})$, and $(x_1^3, x_2^3) = (2.5\,\text{years}, 10.46\,\text{years})$. The earliest time interval captures the rapid early relaxation, and the last time interval captures the longer-term relaxation that is expected to proceed at much slower rates. The last time interval finishes at the time of the M7.2 4 April 2010 El Mayor - Cucapah earthquake in order to avoid any perturbations from that event.

Model misfit for each of the six laterally homogeneous models prescribed in Figure 5 in these time periods is shown in Figure S-5 for horizontal and vertical components. The corresponding model misfit averaged over all time periods is shown in Figure 7. These result from 200000 realizations of random afterslip distributions as described in section 3.2. All patterns are summarized in terms of the total potency (ie., summed slip times area) of

the afterslip model. The scatter for any given model arises from different combinations of slip that give rise to the same potency; for a given potency, some models perform better than others. The best-performing models are Model 1 and Model 3, with steady-state mantle viscosities of $\eta_1 = 10^{19}$ and 4×10^{19} Pa s, respectively..

5.3. Laterally heterogeneous models

As a first step towards obtaining an improvement over laterally homogeneous models, I explore hybrid 2D viscoelastic structures consisting of Model 1 structure in one domain (northeast or southwest domain in Figure 1) and Model 3 structure in the other domain. I find that a hybrid 2D structure, consisting of Model 3 structure in the northeast domain and Model 1 structure in the southwest domain, yields a slightly better RMS v fit than that of Model 1 (Figure 7), but the alternative combination (Model 3 structure in the southwest domain and Model 1 structure in the northeast domain) performs worse. Despite the apparent similarity in performance (RMS v = 0.262 mm/yr for the laterally homogeneous Model 1 versus 0.252 mm/yr for the hybrid model), an F-test indicates that the hybrid model is an improvement over the laterally homogeneous model at nearly the 100% level. This follows from the definition of the F-statistic

$$F = \frac{\left[(\mathrm{RMS\,v}_1)^2 - (\mathrm{RMS\,v}_2)^2\right]/(p_2 - p_1)}{(\mathrm{RMS\,v}_2)^2/(n - p_2)} \tag{15}$$

where $p_1 = 5$ is the number of independent parameters in one laterally homogeneous model (variable Kelvin and Maxwell viscosities in the mantle asthenosphere and mantle lithosphere; variable Maxwell viscosity in the lower crust); $p_2 = 10$ is the number of independent parameters in a trial hybrid structure; $n = 765$ is the number of independent data (109×2 horizontal velocities and 37 vertical velocities observed in three time periods);

RMS v_1 = 0.262 mm/yr and RMS v_2 = 0.252 mm/yr. This yields $F = 12.2$, which is more than 99.9% significant.

I examine a wider range of 2D hybrid models using the Model 1 and Model 3 structures as a guide. I parameterize trial viscoelastic structures in the southwest domain as Model 1 structure modified such that η_1 below 43 km depth may vary from 1.25×10^{18} to 4×10^{19} Pa s, with the ratio η_2/η_1 fixed at the value 4.17. Viscoelastic structures in the northeast domain are parameterized as Model 3 structure such that η_1 below 43 km depth may vary from 1.0×10^{19} to 3.2×10^{20} Pa s, with the ratio η_2/η_1 fixed at the value 10.

The overall misfit RMS v is evaluated as a function of NE-domain η_1 and SW-domain η_1. For each 2D viscoelastic structure I obtain the minimum RMS v resulting from 200000 random afterslip models. The pattern shown in Figure 8 depicts the minimum RMS v as a function of the trial viscoelastic parameters. All viscoelastic models within the range considered in Figure 8 fit the data better than a null model, i.e., one with no relaxation ($u_{\rm rel} = 0$), which has RMS v = 0.36 mm/yr. The smallest RMS v is achieved with SW-domain $\eta_1 = 10^{19}$ Pa s and NE-domain $\eta_1 = 4 \times 10^{19}$ Pa s. The hybrid viscoelastic structure associated with the smallest RMS v (black triangle in Figure 8), which I shall refer to as the 'optimal 2D viscoelastic structure', is depicted in Figure 9.

It is identical to the hybrid of the two best laterally homogeneous models − the Model 1 + Model 3 structure presented in Figure 7.

The discrimination of laterally variable structure from laterally homogeneous structures is possible because of the use of both horizontal and vertical postseismic motions. This is illuminated by the pattern of horizontal and vertical velocity rms misfits, RMS v_H and RMS v_U (Figure S-6). The optimal 2D viscoelastic structure is a compromise among

the fits of horizontal and vertical data among different time periods, which collectively constrain both the NE-domain and SW-domain η_1 more tightly than any single data type or time period alone. An F-test indicates that the optimal structure is significantly better at the 99% level than any model with RMS v > 0.255. This suggests that the NE-domain η_1 lies within the range $2.5 - 5 \times 10^{19}$ Pa s, i.e., about 2.5 to 5 times higher than the SW-domain η_1.

Model time series and velocity vectors for the optimal 2D viscoelastic structure are shown in Figures 2 and 3, respectively. These time series contain only transient signals, i.e. those generated by viscoelastic relaxation, afterslip, and the coseismic step at the time of the Hector Mine quake. They generally capture the observed rapid early transient and much longer slow transient over the subsequent decade.

The juxtaposed mantle domains of contrasting rheology predict different postseismic flow patterns at depth. This is demonstrated by comparing depth-dependent cumulative postseismic displacements for laterally homogeneous and laterally heterogeneous models. The latter differs from the former via the reduced mantle viscosities η_1 and η_2 assigned to the southwest domain. Comparing Figures S-7a and S-7b for these two cases, the effect of its relatively low viscosity is to amplify postseismic displacements within the southwest domain and the proximal part of the northeast domain.

5.4. Independent mantle viscosity estimates

The steady-state viscosity pattern under the two domains is compared with independent estimates in Figure 9. The mantle lithosphere viscosity of 2×10^{20} Pa s for the northeast domain agrees with the range obtained by *Behr and Hirth* [2014] for mantle xenoliths of the Cima volcanic field. The mantle asthenosphere viscosity of 4×10^{19} Pa s is within

the wide range obtained for Basin and Range xenoliths [*Ave'Lallemant et al.*, 1980] as interpreted in Figure 8 of *Behr and Hirth* [2014]. It agrees well with the range of 3 to 5×10^{19} Pa s obtained by *Freed et al.* [2012] using a joint transient and non-linear steady-state rheology model to interpret the first 7 years post-Hector Mine postseismic deformation. Under the northeast domain, the mantle asthenosphere viscosity estimate of 10^{19} Pa s agrees well with the range 8 to 10×10^{18} Pa s estimated by *Smith-Konter et al.* [2014] using a viscoelastic earthquake cycle model to interpret tide gauge measurements.

The transient viscosity of 4×10^{18} Pa s for the northeast-domain mantle asthenosphere is comparable with the range ~ 3 to 10×10^{18} Pa s obtained by *Hammond et al.* [2010] using a Maxwellian rheology model to interpret the post-Hector Mine relaxation pattern in southern Nevada from 1999 to 2009. These viscosity estimates, however, are much higher than the $\sim 10^{18}$ Pa s obtained by *Kaufmann and Amelung* [2000] and *Cavalié et al.* [2007] for the response of the Lake Mead, Nevada, region to changes in surface loads using leveling and InSAR data, respectively. This could indicate additional lateral variations within the northeast domain or that a non-linear rheology (see next section) combined with a relatively high strain rate is applicable to the relaxing mantle beneath Lake Mead following abrupt lake level changes.

6. Physical interpretation of laterally heterogeneous rheology

The preceding results imply that the mantle of the central Mojave Desert is much stronger than the mantle of the western Mojave Desert and the region surrounding the San Andreas fault. Factors affecting the effective viscosity of ductile rock include temperature, strain rate, and water concentration [e.g. *Bürgmann and Dresen*, 2008]. For non-linear power-law creep, the appropriate constitutive equation for olivine in the shallow upper

mantle is [*Hirth and Kohlstedt*, 2003; *Karato and Jung*, 2003]

$$\dot{\epsilon} = A\sigma^n \ (C_{OH})^r \ e^{-H^*/RT}, \quad H^* = Q^* + PV^* \tag{16}$$

where $\dot{\epsilon}$ is the strain rate, A is a constant, σ is the deviatoric stress, n is the stress exponent, C_{OH} is the water concentration, r is the water fugacity exponent, H^* is the activation enthalpy, Q^* and V^* are the activation energy and volume, respectively, P is pressure, T is absolute temperature, and R is the gas constant. n, A, Q^* and V^* may be determined experimentally. The effective viscosity is one-half the ratio of stress to strain rate:

$$\eta_{\text{eff}} = \frac{1}{2} A^{-1/n} \, \dot{\epsilon}^{(1-n)/n} \ (C_{OH})^{-r/n} \ e^{-H^*/nRT} \tag{17}$$

Based on eqn 17 , the lower value of steady-state viscosity in the southwest domain (Figure 9) could imply either higher mantle temperature, a higher strain rate, or higher water concentration. Surface heat flow is a guide to mantle temperature. Remarkably, the heat flow values (Figure 6a) tend to be lower in the southwest domain, where the steady-state mantle viscosity is lower (Figure 9). This is recast in Figure 6b, where the heat flow values are laterally averaged along the N40°W direction and plotted along the N50°E profile distance. The laterally averaged heat flow values are much lower where the mantle viscosity is lower. Heat flow depends upon numerous factors, chiefly crustal thickness, radiogeneic heat production in the crust, and temperature at the crust-mantle boundary [e.g. *Afonso and Ranalli*, 2004]. Neither the crustal thickness nor the lithospheric thickness varies greatly across the Mojave Desert and adjacent San Andreas fault zone [*Richards-Dinger and Shearer*, 1997; *Lekic et al.*, 2011]. However, advective heat transfer from magmatic sources is believed to play an important combined role with lithospheric thinning in the Basin and Range [e.g. *Morgan and Gosnold*, 1989; *Mareschal and Bergantz*, 1990]. An

uncertain part of the high heat flow in the northeast domain reflects such advective heat transfer. A further constraint is provided by uppermost mantle seismic velocities, which are lower in the uppermost $\sim$ 200 km of the mantle of the northeast domain than southwest domain [*Yang et al.*, 2008; *Schmandt and Humphreys*, 2010]. If temperature is the dominant factor shaping the seismic velocity pattern, then mantle temperature in the upper $\sim$ 200 km is higher in the northeast domain, consistent with surface heat flow. Figure 6 then implies that the estimated steady-state mantle viscosity is anti-correlated with mantle temperature and thus shaped by factors other than temperature.

I propose that water concentration in the shallow mantle is an important factor affecting mantle viscosity around southern California. Its capability for explaining the laterally variable steady-state viscosity is demonstrated with viscosity profiles using either a water-saturated olivine rheology or a 'damp' olivine rheology and identical temperature profiles (Figure 10). C_{OH} values in the water-saturated case are from Table 3 of *Dixon et al.* [2004], which have $C_{OH} = 1361$ in the shallow asthenosphere and increasing with depth. The damp viscosity profile is derived from assigning C_{OH} values 18% of the water-saturated values. This is consistent with $C_{OH} = 250$ ppm H/Si obtained by *Behr and Hirth* [2014] for shallow mantle xenoliths from the Cima volcanic field, which is located in the northeast domain.

From Figure S-8, the strain rates appropriate for the southwest and northeast domains are $\dot{\epsilon} \sim 6 \times 10^{-15}$/s and 2×10^{-15}/s, respectively. The viscosity profiles in Figure 10 are calculated for strain rates of 10^{-14}/s and 10^{-15}/s for lower crust and mantle materials and additionally 2×10^{-15}/s in the mantle. Whether these crustal strain rates are applicable to the underlying mantle is uncertain, but I consider it likely that the mantle strain rates do

not exceed these values. Both differing strain rate and hydration level appear necessary to explain the factor of ~ 4 difference in steady-state mantle viscosity η_1 between the two domains. Although water-saturated and damp viscosity profiles at a given strain rate differ by only a factor of ~ 2, water-saturated olivine at $\dot{\epsilon} = 2 \times 10^{-15}$/s underpredicts η_1 of the northeast domain, and damp olivine at $\dot{\epsilon} = 6 \times 10^{-15}$/s overpredicts η_1 of the southwest domain. This suggests that water-saturated olivine and damp olivine mantle (combined with either felsic granulite or mafic granulite in the lower crust) best describe the average compositions within the southwest and northeast domains, respectively.

Uncertainties in the above analysis include the extrapolation of laboratory flow laws to geologic strain rates, the extrapolation of surface strain rates to mantle depths, and the use of 2.5D modeling, where only 2D structures are considered. The latter clearly does not permit 3D variations such as the likely presence of very low viscosity rock around the Salton Sea, but it accounts for first-order differences in structure in two domains parallel to the trend of the San Andreas fault.

7. Discussion

7.1. Afterslip

The distribution of afterslip may be derived from the set of models derived for the optimal viscoelastic structure. A Bayesian approach based on a-priori model uncertainty and a likelihood function is possible [*Minson et al.*, 2013], but here I take a simpler approach. Using the misfit measure RMS v for the optimal 2D viscoelastic structure, the 100 best afterslip models have approximately the same fit to the data (inset of Figure S-9), and I take the mean of these 100 models. The resulting afterslip distribution, i.e., the limit of $u_{\mathrm{aft}}(t)$ for large t, is shown in Figure S-9. It is characterized by relatively

deep slip (> 15 km depth) along the northwest segment and part of the southeast segment. The northeast segment has relatively little afterslip despite the fact that a great many aftershocks occurred beneath it [e.g. *Hauksson et al.*, 2002]. The obtained afterslip distribution is consistent with the tendency of joint seismic-geodetic or purely geodetic models to place relatively large and deep coseismic slip along the northernmost part of the northwest segment [e.g. *Ji et al.*, 2002; *Kaverina et al.*, 2002; *Price and Bürgmann*, 2002].

At sites within 25 km of the Hector Mine rupture surface, viscoelastic relaxation contributes no more than one-quarter of the postseismic motions during the first 0.5 year (Figure 3). Hence afterslip accounts for most of the near-field horizontal deformation during the first 0.5 year. At near-field campaign GPS sites of the 'Emerson Transect', *Savage et al.* [2003] find that post-Hector Mine horizontal motions fit with a time series of the form $a + b + c\exp(-t/d)$ yield a decay time $d = 0.32 \pm 0.18$ year. The preferred Burgers body model of *Pollitz* [2003], who interpreted postseismic deformation at near and intermediate-field sites with a model of viscoelastic relaxation only, has an estimated transient mantle viscosity (i.e., Kelvin component of the rheology) of 1.6×10^{17} Pa s, equivalent to a material relaxation time of 0.07 years. This is near the low end of the range of d estimated by *Savage et al.* [2003]. I have re-estimated the near-field relaxation times using the two closest continuous GPS sites to the Hector Mine rupture that were operational at the time of the earthquake: LDES and CTMS. Fitting of the first 2.5 years of their horizontal time series with curves of the form

$$\text{displacement} = A + Bt + C\exp(-t/\tau_1) + D\exp(-t/\tau_2) \tag{18}$$

yields $\tau_1 = 1.43 \pm 0.27$ year and $\tau_2 = 0.065 \pm 0.014$ year. The fits of the parametric form of eqn 18 to LDES, CTMS, and far-field site BUST are shown in Figure 11. The solid and dashed curves indicate the fits obtained using all parameters or all parameters except the D (i.e., rapid relaxation) term, respectively. Comparison between these curves indicates that postseismic deformation governed by the smaller time constant is about 25% and 50% of the net deformation during the first 0.5 years at CTMS and LDES, respectively, and a negligible fraction at BUST. Since this is qualitatively consistent with the relative contributions of afterslip and relaxation during the first 0.5 years (Figure 3), it is tempting to interpret the smaller time constant as associated entirely with afterslip. However, Figure 3 suggests that afterslip contributes about 50% and 65% of the displacement accumulated during the first 0.5 year at CTMS and LDES, respectively, so the remainder may be attributable to relaxation with a time constant much smaller than 0.5 year, possibly as small as 0.065 year. Model 3 (Figure 5) is the northeast-domain part of the optimal 2D viscoelastic structure and envelopes the Hector Mine rupture area. The Kelvin element of Model 3 has a material relaxation time of 1.81 year, which is close to $\tau_1 = 1.43$ year obtained in the parameteric fits. The Maxwell element of Model 3 has a material relaxation time of 18.1 years.

An interpretation consistent with these results is that postseismic deformation is governed by a combination of afterslip with an exponential decay time of $\sim$ 0.07 to 0.32 years, combined with relaxation at several timescales: $\sim$ 0.07, 1.8, and 18 years. The first and second relaxation timescales are those inferred by *Pollitz* [2003], while the second and third relaxation times are those inferred here for the northeast domain (Figure 9). If

three time constants are indeed needed to describe the relaxation, then the Burgers body model is not wholly adequate for this purpose [e.g. *Hetland and Hager*, 2005].

7.2. Pre-Landers deformation rates

A product of fitting model time series to observed time series is the pre-Landers velocity field, which is a variable in the fit described by eqn 1. The horizontal velocity field resulting from fitting with the optimal 2D viscoelastic structure is shown in Figure S-8a. Away from the plate boundary zone it is very close to the North American plate motion in the NA12 reference frame [*Blewitt et al.*, 2013].

The estimated pre-Landers velocity field exhibits right-lateral strain accumulation along the San Andreas fault system and to a lesser extent within the ECSZ. The horizontal strain rate field is derived from it using the methodology of *Pollitz and Vergnolle* [2006]. This yields the magnitudes and directions of the principle strain rates (e.g., axes of maximum contractile and tensile strain) and the rotation rate (Figure S-8b,c). These strain rates are compared with estimates of pre-Landers strain rates determined from regional trilateration networks operating during the period 1973 - 1990 [*Savage and Prescott*, 1973; *Savage et al.*, 2001] in Figure S-8c. The two estimates of pre-Landers strain rates are in reasonable agreement. The estimates based on our quasi-static modeling predict strain rates increasing from west to east in the Barstow net and decreasing from west to east in the Garlock net, in agreement with observed trends from the trilateration nets, though the trilateration-based strain rates in the Garlock net exhibit a smaller decrease. The rates based on the quasi-static model are $\sim 50\%$ smaller than the trilateration-based rates in the Garlock central and Garlock east subnets.

If this discrepancy is real, it may imply a shortcoming of the quasi-static model in this area. The pre-Landers 'background' velocities will trade off with the steady-state mantle viscosity. A larger steady-state viscosity in a localized area will produce a larger background velocity because the mantle relaxation and the background velocity are the primary factors that shape the tail end of all post-Hector Mine time series; if the velocity contributed by the relaxation decreases, the background velocity must correspondingly increase. The Garlock subnet strain rates at $\sim 35.5°$N are interpolated velocity gradient fields that factor in velocities in the ECSZ both north of $\sim 36.0°$N and south of $\sim 35.0°$N. I find that a 3 mm/yr decrease in northward background velocity north of 36.0°N, or a 3 mm/yr increase south of 35.0°N, yields a greater model north-south contractile strain around the eastern Garlock and thus explains the discrepancy with the trilateration-measured strain. However, a 3 mm/yr tradeoff with steady-state relaxation is unlikely since the overall relaxation signal at late times is less than 2 mm/yr (Figure 3). It is possible that the central and Garlock network strains are influenced by local effects such as steady deep slip beneath the Garlock fault; this process would contribute to the *Savage et al.* [2001] trilateration measurements but not the GPS-derived strain estimated in this study since the GPS measurements can resolve only relatively long-wavelength strain in this area. Another explanation for the discrepancy may be postseismic relaxation following the 1952 Mw 7.3 Kern County earthquake [*Bawden*, 2001]. Forward models done by *Hearn et al.* [2013] indicate transient motions of a few mm/yr in the Garlock central and east subnet areas (depending on the assumed viscoelastic model) in the 1970s that diminish gradually with time. This would have led to strain transients on the order of 10^{-8} per year that might have contributed to the 'background strain rate' measurements analyzed

by *Savage et al.* [2001] but less so to recent GPS measurements. The size and pattern of the 1952-earthquake transient deserves further study.

7.3. Relaxation pattern in southern Nevada and Los Angeles Basin

Freed et al. [2007] showed that transient motions near Yucca Mountain, southern Nevada, demand mantle relaxation during the 7 years following the Hector Mine earthquake. In that region (their Figure 1), they find transient horizontal motions $\sim$ 0.6 mm/yr. My estimate of the transient horizontal velocity field for these 7 years based on the optimal 2D viscoelastic structure, using only the first 7 years of observed time series, is shown in Figure 12. The size of the observed transient in southern Nevada using the present estimation procedure is $\sim$ 0.4 mm/yr. The rates are small and vary substantially over $\sim$ 50 lateral distance, despite the $>$ 200 km distance of the southern Nevada sites from the Hector Mine source, because the area is located just east of a node in the postseismic displacement field. The viscosity of $10^{18.5}$ inferred for this region by *Hammond et al.* [2010] using a Maxwell rheology is similar to the Kelvin viscosity of 4×10^{18} Pa s on the optimal 2D viscoelastic structure.

In the Los Angeles Basin I discern a small observed NW transient in this area $\sim 0.5-1$ mm/yr, a result consistent with the observation of *Argus et al.* [2005]. The westward component of the transient in this region is directly implied by the concave upward curvature of east-component time series such as LVMS and CSN1 (Figure 2). The modeled transient on the 2D structure is also to the NW (Figure 12) and matches the amplitude of the observed transient. Hence, to explain the these motions with mantle relaxation, lateral variations within the southwest domain, e.g., higher viscosity mantle west of the San Andreas fault [*Spinler et al.*, 2010], need not be invoked.

7.4. Implications of rheology structure

Taken at face value, the damp versus water-saturated olivine envisioned for the northeast and southwest domains implied by Figure 10 is consistent with the extraction of water and incompatible elements when producing partial melt which is then transported upward to produce igneous rocks or extruded as surface volcanics. This is a consequence of the high solubility of water in the melt compared to the solid fraction [e.g. *Kohlstedt et al.*, 1996; *Zhao et al.*, 2004]. This process has been proceeding continually in the southwestern Basin and Range Province since 24-22 Ma, and the late Cenozoic activity effectively terminates at the border dividing the two domains [*Glazner et al.*, 2002]. In this interpretation, water delivered by plate subduction to the western US mantle [e.g. *Hyndman et al.*, 2005; *Dixon et al.*, 2004] has remained essentially intact under the southwest domain since the cessation of subduction $\sim$ 30 Ma [*Atwater and Stock*, 1998].

Seismic wave attenuation is expected to be very sensitive to water content [*Karato and Jung*, 1998; *Aizawa et al.*, 2008]. Joint phase velocity and attenuation structure of the western US have been obtained by *Lin et al.* [2012] based on interpretation of Rayleigh wave amplitudes with Helmholtz tomography. Constraining seismic wave attenuation independently from systematic focussing / defocussing effects is difficult, and *Lin et al.* [2012] present surface wave amplification results both without and with a correction for these effects. The high-resolution results at 60 sec period, which is sensitive to asthenosphere structure between 50 and 150 km depth, in their Figure 11 exhibit features that appear robust, i.e., they appear regardless of whether a local amplification correction is made or not. Most of the western US coastal region exhibits relatively high amplitude decay (low Q). As shown by laterally averaged values of amplitude decay estimated by

Lin et al. [2012], southwestern California – over an area approximately coinciding with the southwest domain – is more highly attenuating than the adjacent southern Basin and Range (Figure 13). This pattern for the southern California asthenosphere and elsewhere, e.g., relatively low amplitude decay (high Q) inferred at 60 sec period below the Yellowstone hotspot (Figure 11 of *Lin et al.* [2012]), run counter to expectations based on heat flow. They may all be part of a systematic pattern where lateral variations in hydration, resulting chiefly from the pattern of igneous and volcanic activity over the past 20 Myr, shape the mechanical strength and seismic wave attenuation of the western US asthenosphere more strongly than temperature.

Relatively low viscosity of the southwest domain mantle is consistent with interpretations of downwelling mantle beneath the Transverse Ranges [e.g. *Bird and Rosenstock*, 1984; *Sheffels and McNutt*, 1986; *Humphreys and Clayton*, 1990]. High-velocity mantle extending to $\sim$ 150 km depth [*Yang and Forsyth*, 2006] or deeper [e.g. *Humphreys and Clayton*, 1990] is interpreted using thin sheet models to result from convective instability below the Transverse Ranges arising around the time of onset of crustal convergence 5 Ma [*Houseman et al.*, 2000; *Billen and Houseman*, 2004]. The steady-state mantle viscosity (η_1 deeper than 43 km) of the present study is equivalent to the asthenosphere viscosity of *Houseman et al.* [2000] and *Billen and Houseman* [2004], who regard the asthenosphere viscosity as negligible compared with the viscosity of the lithospheric mantle. Estimated lithospheric mantle viscosity to replicate the topography and width of the San Gabriel Mountains is $\sim 10^{21}$ Pa s [*Billen and Houseman*, 2004]; it is $\lesssim 10^{20}$ Pa s to form the Transverse Ranges downwelling over the past 5 Myr [*Houseman et al.*, 2000]. The southwest domain η_1 of 10^{19} is much less than both estimates and is thus consistent with the

thin sheet models of convective instability. The viscosity of the mantle lid (i.e., η_1 between 30 and 43 km depth in the optimal 2D viscoelastic structure) is not independently constrained in the grid search of section 5.3, but its value of 5×10^{19} Pa s is close to the *Houseman et al.* [2000] estimate of 10^{20} Pa s.

8. Conclusions

The time-dependent GPS velocity field obtained from 15 years of postseismic relaxation data from the 1992 M7.3 Landers and 1999 M7.1 Hector Mine earthquakes constrains the viscoelastic structure of the southern California lower crust and upper mantle. Application of a 2.5D spectral element model of quasi-static deformation enables the determination of 2D viscoelastic structure; it varies in the depth and N50°E direction but is uniform in the N40°W direction. The use of near-field and far-field observations, as well as the vertical component of surface motions, permits the discrimination of viscoelastic relaxation from afterslip and helps resolve both depth-dependent and laterally variable viscoelastic structure.

Joint modeling of viscoelastic relaxation and afterslip yields a viscoelastic structure characterized by a relatively weak mantle of a 'southwest domain' comprising the western Mojave Desert and the San Andreas fault zone. Its steady-state viscosity is ~ 4 times lower than that of an adjacent northeast domain that comprises the central Mojave Desert, including the Landers and Hector Mine rupture zones. Since heat flow of the southwest domain is on average lower than that of the northeast domain, its lower viscosity is explained via a combination of higher background strain rate and higher water concentration in olivine. This conclusion, based on a non-linear (stress-dependent) rheology, is tentative because of numerous uncertainties, including the extrapolation of

laboratory flow laws to geologic strain rates and the extrapolation of the surface strain rate field to mantle depths. If true, however, it implies that water injected into the mantle during Mesozoic-to-mid-Cenozoic subduction has remained intact under the southwest domain since the cessation of subduction ~ 30 Ma, but not under the northeast domain where continual volcanism for the past ~ 20 Myr has gradually extracted water from the mantle.

The Burgers body rheology model in each domain permits two material mantle relaxation times. They equal 1.81 and 18.1 years in the northeast domain, which envelopes the Hector Mine rupture area. Much shorter timescales are indicated by the *Savage et al.* [2003] analysis of the campaign GPS Emerson Transect (0.32 ± 0.18 year) and by examination of continuous time series near the Hector Mine rupture (0.065 ± 0.014 year). Since such short-timescale deformation is absent at remote sites, it is interpreted as associated predominantly with afterslip. However, a small part of the mantle or lower crust relaxation may have occurred with a similarly short timescale. If so, then a generalized Burgers body model [e.g. *Ivins*, 1996; *Hetland and Hager*, 2005] may be necessary to more fully capture the details of the relaxation.

Acknowledgements I thank Fan-Chi Lin for providing the amplitude decay results used in Figure 13, and Jim Savage, Wayne Thatcher, and Roland Bürgmann for their comments on a preliminary draft. This paper benefitted from the constructive criticisms of Gareth Funning, an anonymous reviewer, and the Associate Editor. GPS time series used in this study are extracted from http://geodesy.unr.edu/gps_timeseries/tenv3/NA12/

References

Afonso, J. C., and G. Ranalli, Crustal and mantle strengths in continental lithosphere: is the jelly sandwich model obsolete?, *Tectonophysics*, *394*, 221–232, 2004.

Aizawa, Y., A. Barnhoorn, U. Faul, J. F. Gerald, and I. Jackson, The influence of water on seismic wave attenuation in dunite: an exploratory study, *J. Petrology*, *49*, 841–855, 2008.

Argus, D. F., M. B. Heflin, G. Peltzer, F. Crampé, and F. H. Webb, Interseismic strain accumulation and anthropogenic motion in metropolitan Los Angeles, *J. Geophys. Res.*, *110*, doi: 10.1029/2003JB002934, 2005.

Atwater, T., and J. M. Stock, Implications of plate tectonics for the Cenozoic tectonic evolution of western North America, *Geol. Soc. Am. Bull.*, *81*, 3513–3536, 1998.

Ave'Lallemant, H., J. Mercier, N. Carter, and J. Ross, Rheology of the upper mantle: inferences from peridotite xenoliths, *Tectomophysics*, *70*, 85–113, 1980.

Bawden, G. W., Source parameters for the 1952 Kern County earthquake, California: A joint inversion of leveling and triangulation observations, *J. Geophys. Res.*, *106*, 771–785, 2001.

Behr, W. M., and G. Hirth, Rheological properties of the mantle lid beneath the Mojave region in southern California, *Earth Planet. Sci. Lett.*, *393*, 60–72, 2014.

Billen, M. I., and G. A. Houseman, Lithospheric instability in obliquely convergent margins: San Gabriel Mountains, southern California, *J. Geophys. Res.*, *109*(B1), B01,404, doi:10.1029/2003JB002605, 2004.

Bird, P., and R. W. Rosenstock, Kinematics of present crust and mantle flow in southern California, *Geol. Soc. Am. Bull.*, *95*(8), 946–957, 1984.

Blewitt, G., C. Kreemer, W. C. Hammond, and J. M. Goldfarb, Terrestrial reference frame NA12 for crustal deformation studies in North America, *J. Geodynamics*, *72*, 11–24, 2013.

Bürgmann, R., and G. Dresen, Rheology of the lower crust and upper mantle: Evidence from rock mechanics, geodesy, and field observations, *Ann. Rev. Earth Planet. Sci.*, *36*, 531–567, 2008.

Cavalié, O., M.-P. Doin, C. Lasserre, and P. Briole, Ground motion measurement in the Lake Mead area, Nevada, by differential synthetic aperture radar interferometry time series analysis: Probing the lithosphere rheological structure, *J. Geophys. Res.*, *112*, B03,403, doi:10.1029/2006JB004344, 2007.

Chopra, P. N., High-temperature transient creep in olivine rocks, *Tectonophysics*, *279*, 93–111, 1997.

Cohen, S., A multilayer model of time dependent deformation following an earthquake on a strike slip fault, *J. Geophys. Res.*, *87*, 5409–5421, 1982.

Cohen, S., Evaluation of the importance of model features for cyclic deformation due to dip-slip faulting, *Geophys. J. Int.*, *119*, 831–841, 1994.

Cohen, S., Viscoelastic postseismic rebound from strike-slip earthquakes in regions of oblique plate convergence, *Bull. Seismol. Soc. Am.*, *90*, 1318–1322, 2000.

Cohen, S. C., Numerical models of crustal deformation in seismic zones, in *Advances in Geophysics*, vol. 41, edited by R. Dmowska and B. Saltzman, pp. 133–231, Academic Press, San Diego, 1999.

Dixon, J. E., T. H. Dixon, D. R. Bell, and R. Malservisi, Lateral variation in upper mantle viscosity: Role of water, *Earth Planet. Sci. Lett.*, *222*, 451–467, 2004.

Fialko, Y., Evidence of fluid-filled upper crust from observations of postseismic deformation due to the 1992 mw7.3 Landers earthquake, *J. Geophys. Res.*, *109*, doi:10.1029/2004JB002985, 2004.

Freed, A. M., and R. Bürgmann, Evidence of powerlaw flow in the Mojave Desert mantle, *Nature*, *430*, 548–551, 2004.

Freed, A. M., R. Bürgmann, and T. Herring, Far-reaching transient motions after Mojave earthquakes require broad mantle flow beneath a strong crust, *Geophys. Res. Lett.*, *34*, doi:/10.1029/2006GL029155, 2007.

Freed, A. M., G. Hirth, and M. D. Behn, Using short-term postseismic displacements to infer the ambient deformation conditions of the upper mantle, *J. Geophys. Res.*, *117*, B01,409, doi:10.1029/2011JB008562, 2012.

Glazner, A. F., J. D. Walker, J. M. Bartley, and J. M. Fletcher, Cenozoic evolution of the Mojave block of southern California, in *Geologic Evolution of the Mojave Desert and Southwestern Basin and Range*, vol. 195, edited by A. F. Glazner, J. D. Walker, and J. M. Bartley, pp. 19–41, Geological Society of America, 2002.

Goes, S., and S. van der Lee, Thermal structure of the Noath American uppermost mantle inferred from seismic tomography, *J. Geophys. Res.*, *107*, doi: 10.1029/2000JB000049, 2002.

Gourmelen, N., and F. Amelung, Postseismic mantle relaxation in the Central Nevada Seismic Belt, *Science*, *310*, 1473–1476, 2005.

Hammond, W. C., C. Kreemer, and G. Blewitt, Geodetic constraints on contemporary deformation in the northern Walker Lane: 3, Central Nevada Seismic Belt postseismic relaxation, in *Late Cenozoic Structure and Evolution of the Great Basin Sierra Nevada*

Transition, pp. 33–54, Geological Society of America Special Paper, 2009.

Hammond, W. C., C. Kreemer, G. Blewitt, and H.-P. Plag, Effect of viscoelastic postseismic relaxation on estimates of interseismic crustal strain accumulation at Yucca Mountain, Nevada, *Geophys. Res. Lett.*, *37*, L06,307,doi:10.1029/2010GL042795, 2010.

Hauksson, E., L. M. Jones, and K. Hutton, The 1999 mw 7.1 Hector Mine, California, earthquake sequence: Complex conjugate strike-slip faulting, *Bull. Seismol. Soc. Am.*, *92*, 1154–1170, 2002.

Hearn, E. H., S. McClusky, S. Ergintav, and R. E. Reilinger, Izmit earthquake postseismic deformation and dynamics of the North Anatolian Fault Zone, *J. Geophys. Res.*, *114*, B08,405, doi:10.1029/2008JB006026, 2009.

Hearn, E. H., F. Pollitz, W. Thatcher, and C. Onishi, How do 'ghost transients' from past earthquakes affect GPS slip rate estimates on southern California faults?, *Geochem. Geophys. Geosys.*, *14*, 828–838, DOI:10.1002/ggge.20080, 2013.

Hetland, E. A., and B. H. Hager, Postseismic and interseismic displacements near a strike-slip fault: a 2D theory for general linear viscoelastic rheologies, *J. Geophys. Res.*, *110*, B10,401, doi:10.1029/2005JB003689, 2005.

Hetland, E. A., and B. H. Hager, The effects of rheological layering on post-seismic deformation, *Geophys. J. Int.*, *166*, 277–292, 2006.

Hines, T. T., and E. A. Hetland, Bias in estimates of lithosphere viscosity from interseismic deformation, *Geophys. Res. Lett.*, *40*, 4260–4265,DOI:10.1002/grl.50839, 2013.

Hirth, G., and D. Kohlstedt, Review of the Upper Mantle and the Mantle Wedge: A View from the Experimentalists, in *Inside the Subduction Factory*, vol. 138, pp. 83–105, American Geophysical Union, 2003.

Houseman, G. A., E. A. Neil, and M. D. Kohler, Lithospheric instability beneath the Transverse Ranges of California, *J. Geophys. Res.*, *105*, 16,237–16,250, doi:10.1029/2000JB900118, 2000.

Hu, Y., and K. Wang, Spherical-Earth finite element model of short-term postseismic deformation following the 2004 Sumatra earthquake, *J. Geophys. Res.*, *117*, B05,404,doi:10.1029/2012JB009153, 2012.

Hu, Y., R. Bürgmann, J. T. Freymueller, P. Banerjee, and K. Wang, Contributions of poroelastic rebound and a weak volcanic arc to the postseismic deformation of the 2011 Tohoku earthquake, *Earth Planet. Sci. Lett.*, *in press*, 2014.

Huang, M.-H., R. Bürgmann, and A. M. Freed, Probing the lithospheric rheology across the eastern margin of the Tibetan Plateau, *Earth Planet. Sci. Lett.*, *396*, 88–96, 2014.

Humphreys, E. D., and R. W. Clayton, Tomographic image of the southern California mantle, *J. Geophys. Res.*, *95*, 19,725–19,746, doi:10.1029/JB095iB12p19725, 1990.

Hyndman, R. D., C. A. Currie, and S. P. Mazzotti, Subduction zone backarcs, mobile belts, and orogenic heat, *GSA Today*, *15*, doi: 10:1130/1052–5173, 2005.

Ivins, E. R., Transient creep of a composite lower crust, 2, a polymineralic basis for rapidly evolving postseismic deformation modes, *J. Geophys. Res.*, *101*, 28,005–28,028, 1996.

Ji, C., D. J. Wald, and D. V. Helmberger, Source description of the 1999 Hector Mine, California, earthquake, Part II: Complexity of slip history, *Bull. Seismol. Soc. Am.*, *92*, 1208–1226, 2002.

Ji, K. H., and T. A. Herring, Correlation between changes in groundwater levels and surface deformation from GPS measurements in the San Gabriel Valley, California, *Geophys. Res. Lett.*, *39*, L01,301, doi:10.1029/2011GL050195, 2012.

Jónsson, S., H. Zebker, P. Segall, and F. Amelung, Fault slip distribution of the 1999 Mw 7.1 Hector Mine, California, Eearthquake Estimated From Satellite Radar and GPS Measurements, *Bull. Seismol. Soc. Am.*, *92*, 1377–1389, 2002.

Jónsson, S., P. Segall, R. Pedersen, and G. Björnsson, Post-earthquake ground movements correlated to pore-pressure transients, *Nature*, *424*, 179–183, 2003.

Karato, S.-I., and H. Jung, Water, partial melting and the origin of the seismic low velocity and high attenuation zone in the upper mantle, *Earth Planet. Sci Lett.*, *157*, 193–207, doi: 10.1016/s0012–821x(98)00034–x, 1998.

Karato, S.-I., and H. Jung, Effects of pressure on high-temperature dislocation creep in olivine, *Philosophical Magazine*, *83*, 401–414, 2003.

Kaufmann, G., and F. Amelung, Reservoir-induced deformation and continental rheology in the vicinity of Lake Mead, Nevada, *J. Geophys. Res.*, *105*, 16,341–16,358, 2000.

Kaverina, A., D. Dreger, and E. Price, The combined Inversion of Seismic and Geodetic Data for the Source Process of the 16 October 1999 Mw 7.1 Hector Mine, California, Earthquake, *Bull. Seismol. Soc. Am.*, *92*, 1266–1280, 2002.

Khazaradze, G., K. Wang, J. Klotz, Y. Hu, and J. He, Prolonged post-seismic deformation of the 1960 great Chile earthquake and implications for mantle rheology, *Geophys. Res. Lett.*, *29*, 2050, doi:10.1029/2002GL015986, 2002.

Kirby, S. H., and A. K. Kronenberg, Strength of the lithosphere: Selected topics, *Rev. Geophys.*, *25*, 1219–1244, doi: 10.1029/RG025i006p01219, 1987.

Kohler, M. D., and P. M. Davis, Crustal thickness variations in southern California from Los Angeles Region Seismic Experiment passive phase teleseismic travel times, *Bull. Seismol. Soc. Am.*, *87*, 1330–1344, 1997.

Kohlstedt, D. L., H. Keppler, and D. C. Rubie, Solubility of water in the α, β, and γ phases of $(Mg,Fe)_2SiO_4$, *Contr. Mineral. Petrol.*, *123*, 345–357, 1996.

Lekic, V., S. W. French, and K. M. Fischer, Lithospheric Thinning Beneath Rifted Regions of Southern California, *Science Express*, p. 10.1126/science.1208898, 2011.

Li, Y.-G., J. E. Vidale, S. M. Day, D. D. Oglesby, and the SCEC Working Team, Study of the 1999 M 7.1 Hector Mine, California, Earthquake Fault Plane by Trapped Waves, *Bull. Seismol. Soc. Am.*, *92*, 1318–1332, 2002.

Lin, F.-C., V. C. Tsai, and M. H. Ritzwoller, The local amplification of surface waves: A new observable to constrain elastic velocities, density, and anelastic attenuation, *J. Geophys. Res.*, *117*, B06,302, doi:10.1029/2012JB009208, 2012.

Mareschal, J., and G. Bergantz, Constraints on thermal models of the Basin and Range province, *Tectonophysics*, *174*, 137–146, 1990.

Minson, S. E., M. Simons, and J. L. Beck, Bayesian inversion for finite fault earthquake source models i – theory and algorithm, *Geophys. J. Int.*, *194*, 1701–1726, doi:10.1093/gji/ggt180, 2013.

Morgan, P., and W. D. Gosnold, Heat flow and thermal regimes in the continental United States, in *Geophysical Framework of the Continental United States*, edited by L. C. Pakiser and W. D. Mooney, 172, pp. 493–522, Geological Society of America, 1989.

Nishimura, T., and W. Thatcher, Rheology of the lithosphere inferred from postseismic uplift following the 1959 Hebgen Lake earthquake, *J. Geophys. Res.*, *108*, 10.1029/2002JB002,191, 2003.

Ozakin, Y., and Y. Ben-Zion, Systematic Receiver Function Analysis of the Moho Geometry in the Southern California Plate-Boundary Region, *Pure Appl. Geophys.*, DOI

10.1007/s00024–014–0924–6, 2014.

Peltzer, G., P. Rosen, F. Rogez, and K. Hudnut, Post-seismic rebound in fault step-overs caused by pore fluid flow, *Science*, *273*, doi: 10.1126/science.273.5279.1202, 1996.

Peltzer, G., P. Rosen, F. Rogez, and K. Hudnut, Post-seismic deformation along the Landers 1992 earthquake surface rupture, *J. Geophys. Res.*, *103*, 30,131–30,145, 1998.

Perfettini, H., and J.-P. Avouac, Modeling afterslip and aftershocks following the 1992 Landers earthquake, *J. Geophys. Res.*, *112*, B07,409, doi:10.1029/2006JB004399, 2007.

Pollitz, F., and W. Thatcher, On the resolution of shallow mantle viscosity structure using post-earthquake relaxation data: Application to the 1999 Hector Mine, California, earthquake, *Geophys. J. Int.*, *115*, Q06,008, doi:10.1029/2010JB007405, 2010.

Pollitz, F. F., Transient rheology of the uppermost mantle beneath the Mojave Desert, California, *Earth Planet. Sci. Lett.*, *215*, 89–104, 2003.

Pollitz, F. F., Transient rheology of the upper mantle beneath central Alaska inferred from the crustal velocity field following the 2002 Denali earthquake, *J. Geophys. Res.*, *110*, B08,407, doi:10.1029/2005JB003672, 2005.

Pollitz, F. F., Post-Earthquake Relaxation Using a Spectral Element Method: 2.5-D Case, *Geophys. J. Int.*, doi: 10.1093/gji/ggu114, 2014.

Pollitz, F. F., and M. Vergnolle, Mechanical deformation model of the western United States instantaneous strain-rate field, *Geophys. J. Int.*, *167*, 421–444, 2006.

Pollitz, F. F., G. Peltzer, and R. Bürgmann, Mobility of the continental mantle : Evidence from postseismic geodetic observations following the 1992 Landers earthquake, *J. Geophys. Res.*, *105*, 8035–8054, 2000.

Pollitz, F. F., C. Wicks, and W. Thatcher, Mantle flow beneath a continental strike-slip fault : Postseismic deformation after the 1999 Hector Mine earthquake, *Science*, *293*, 1814–1818, 2001.

Pollitz, F. F., R. Bürgmann, and W. Thatcher, Illumination of rheological mantle heterogeneity by the M7.2 2010 El Mayor-Cucapah earthquake, *Geochem. Geophys. Geosys.*, *13*, doi: 10.1029/2012GC004139, 2012.

Post, R. L., High-temperature creep of Mt. Burnet Dunite, *Tectonophysics*, *42*, 75–110, 1977.

Price, E., and R. Bürgmann, Interactions between the Landers and Hector Mine, California, earthquakes from space geodesy, boundary element modeling, and time-dependent friction, *Bull. Seismol. Soc. Am.*, *92*, 1450–1469, 2002.

Ranalli, G., *Rheology of the Earth*, Chapman and Hall, London, 1995.

Richards-Dinger, K. B., and P. M. Shearer, Estimating crustal thickness in southern California by stacking PmP arrivals, *J. Geophys. Res.*, *102*, 15,211–15,224, 1997.

Rousset, B., S. Barbot, J.-P. Avouac, and Y.-J. Hsu, Postseismic deformation following the 1999 Chi-Chi earthquake, Taiwan: Implication for lower-crust rheology, *J. Geophys. Res.*, *117*, B12,405,doi:10.1029/2012JB009571, 2012.

Ryder, I., R. Bürgmann, and F. F. Pollitz, Lower crustal relaxation beneath the Tibetan Plateau and Qaidam Basin following the 2001 Kokoxili earthquake, *Geophys. J. Int.*, *197*, doi: 10.1111/j.1365–1246X.2011.05179.x, 2011.

Savage, J. C., Strain accumulation in western United States, *Annu. Rev. Earth Planet. Sci.*, *368*, 11–43, 1983.

Savage, J. C., and W. H. Prescott, Precision of Geodolite distance measurements for determining fault movements, *J. Geophys. Res.*, *78*, 6001–6008, 1973.

Savage, J. C., and J. Svarc, Postseismic deformation associated with the 1992 Mw=7.3 Landers earthqake, southern California, *J. Geophys. Res.*, *102*, 7565–7577, 1997.

Savage, J. C., and J. L. Svarc, Postseismic relaxation and transient creep, *J. Geophys. Res.*, *110*, B11,402, doi:10.1029/2005JB003687, 2005.

Savage, J. C., W. Gan, and J. L. Svarc, Strain accumulation and rotation in the Eastern California Shear Zone, *J. Geophys. Res.*, *106*, 21,995–22,008, 2001.

Savage, J. C., J. L. Svarc, and W. H. Prescott, Postseismic deformation associated with the 1992 landers and 1999 hector mine, california, earthquakes, *J. Geophys. Res.*, *108*, 2432,doi:10.1029/2002JB002330, 2003.

Schmandt, B., and E. Humphreys, Seismic heterogeneity and small-scale convection in the southern California upper mantle, *Geochem. Geophys. Geosys.*, *11*, Q05,004, doi:10.1029/2010GC003042, 2010.

Segall, P., *Earthquake and Volcano Deformation*, Princeton University Press, Princeton, 2010.

Shao, Z., R. Wang, Y. Wu, and L. Zhang, Rapid afterslip and short-term viscoelastic relaxation following the 2008 Mw 7.9 Wenchain earthquake, *Earthquake Sci.*, *24*, 163–175, 2011.

Sheffels, B., and M. McNutt, Role of subsurface loads and regional compensation in the isostatic balance of the Transverse Ranges, California: Evidence for intracontinental subduction, *J. Geophys. Res.*, *91*, 6419–6431, doi:10.1029/JB091iB06p06419, 1986.

Shen, Z.-K., D. Jackson, Y. Feng, M. Cline, M. Kim, P. Fang, and Y. Bock, Postseismic deformation following the Landers earthquake, California, *Bull. Seismol. Soc. Am.*, *84*, 780–791, 1994.

Smith-Konter, B., G. Thornton, and D. Sandwell, Vertical crustal displacement due to inter seismic deformation along the San Andreas fault: Cconstraints from tide gauges, *Geophys. Res. Lett.*, *111*, 10.1002/2014GL060,091, 2014.

Spinler, J. C., R. A. Bennett, M. L. Anderson, S. F. McGill, S. Hreinsdóttir, and A. McCallister, Present-day strain accumulation and slip rates associated with southern San Andreas and eastern California shear zone faults, *J. Geophys. Res.*, *115*, doi: 10.1029/2010JB007424, 2010.

Tape, C., Q. Liu, A. Maggi, and J. Tromp, Seismic tomography of the southern California crust based on spectral-element and adjoint methods, *Geophys. J. Int.*, *180*, 433–462, doi: 10.1111/j.1365–246X.2009.04429.x, 2010.

Thatcher, W., and F. F. Pollitz, Temporal evolution of continental lithospheric strength in actively deforming regions, *GSA Today*, *18*, 4–11, 2008.

Tian, Y., D. Zhao, and J. Teng, Deep structure of southern California, *Phys. Earth Planet. Int.*, *165*, 93–113, 2007.

Wald, D., and T. Heaton, Spatial and temporal distribution of slip for the 1992 Landers, California, earthquake, *Bull. Seismol. Soc. Am.*, *84*, 668–691, 1994.

Wang, K., Y. Hu, and J. He, Deformation cycles of subduction earthquakes in a viscoelastic Earth, *Nature*, *484*, 327–332, 2012.

Wilks, K. R., and N. L. Carter, Rheology of some continental lower crustal rocks, *Tectonophysics*, *182*, doi: 10.1016/0040–1951(90)90342–6, 1990.

Wright, T. J., J. R. Elliott, H. Wang, and I. Ryder, Earthquake cycle deformation and the Moho: Implications for the rheology of the continental lithosphere, *Tectonophysics*, *609*, 504–523, 2013.

Yan, Z., and R. W. Clayton, Regional mapping of the crustal structure in southern California from receiver functions, *J. Geophys. Res.*, *112*, B05,311, doi:10.1029/2006JB004622, 2007.

Yang, Y., and D. W. Forsyth, Rayleigh wave phase velocities, small-scale convection, and azimuthal anisotropy beneath southern California, *J. Geophys. Res.*, *111*, doi:10.1029/2005JB004180, 2006.

Yang, Y., M. H. Ritzwoller, F. C. Lin, M. P. Moschetti, and N. M. Shapiro, Structure of the crust and uppermost mantle beneath the western United States revealed by ambient noise and earthquake tomography, *J. Geophys. Res.*, *113*, B12,310, doi:10.1029/2008JB005833, 2008.

Zhao, Y.-H., S. B. Ginsberg, and D. L. Kohlstedt, Solubility of hydrogen in olivine: dependence on temperature and iron content, *Contr. Mineral. Petrol.*, *147*, 155–161, 2004.

Zhu, L., and H. Kanamori, Moho depth variation in Southern California from teleseismic receiver functions, *J. Geophys. Res.*, *105*, 2969–2980, 2000.

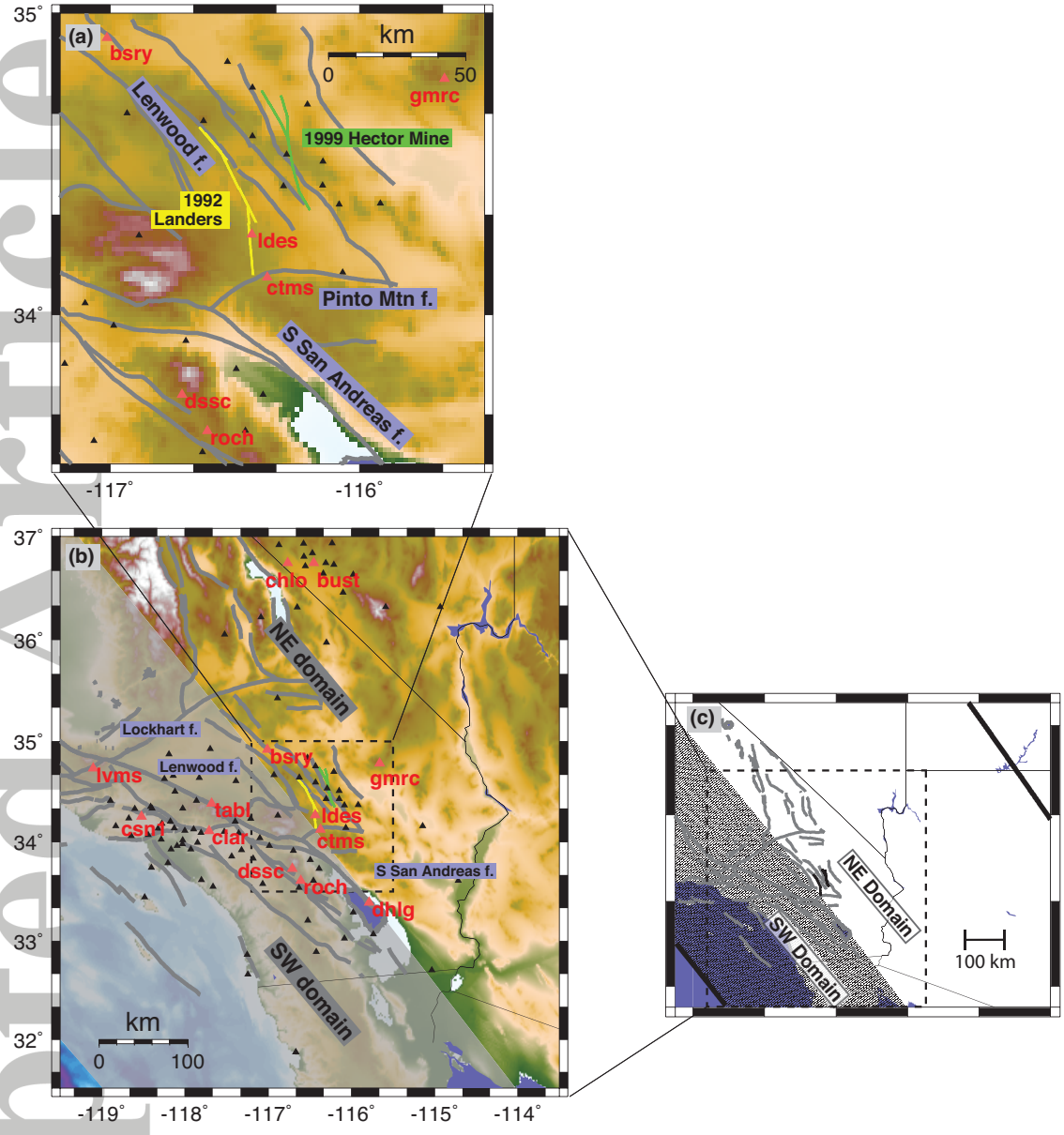

Figure 1. Delineation of southwest and northeast 2D rheological structure domains. The boundary between the two domains lies approximately along the Lockhart-Lenwood faults and the Southern San Andreas fault south of the Pinto Mountain fault. GPS sites are shown with black triangles. Selected stations are highlighted with red triangles and labelled. Yellow and green line denote traces of the 1992 Landers and 1999 Hector Mine earthquake ruptures, respectively. (a) is a closeup of the boxed area in (b). The horizontal boundaries of the model domain are shown in (c) as thick black lines.

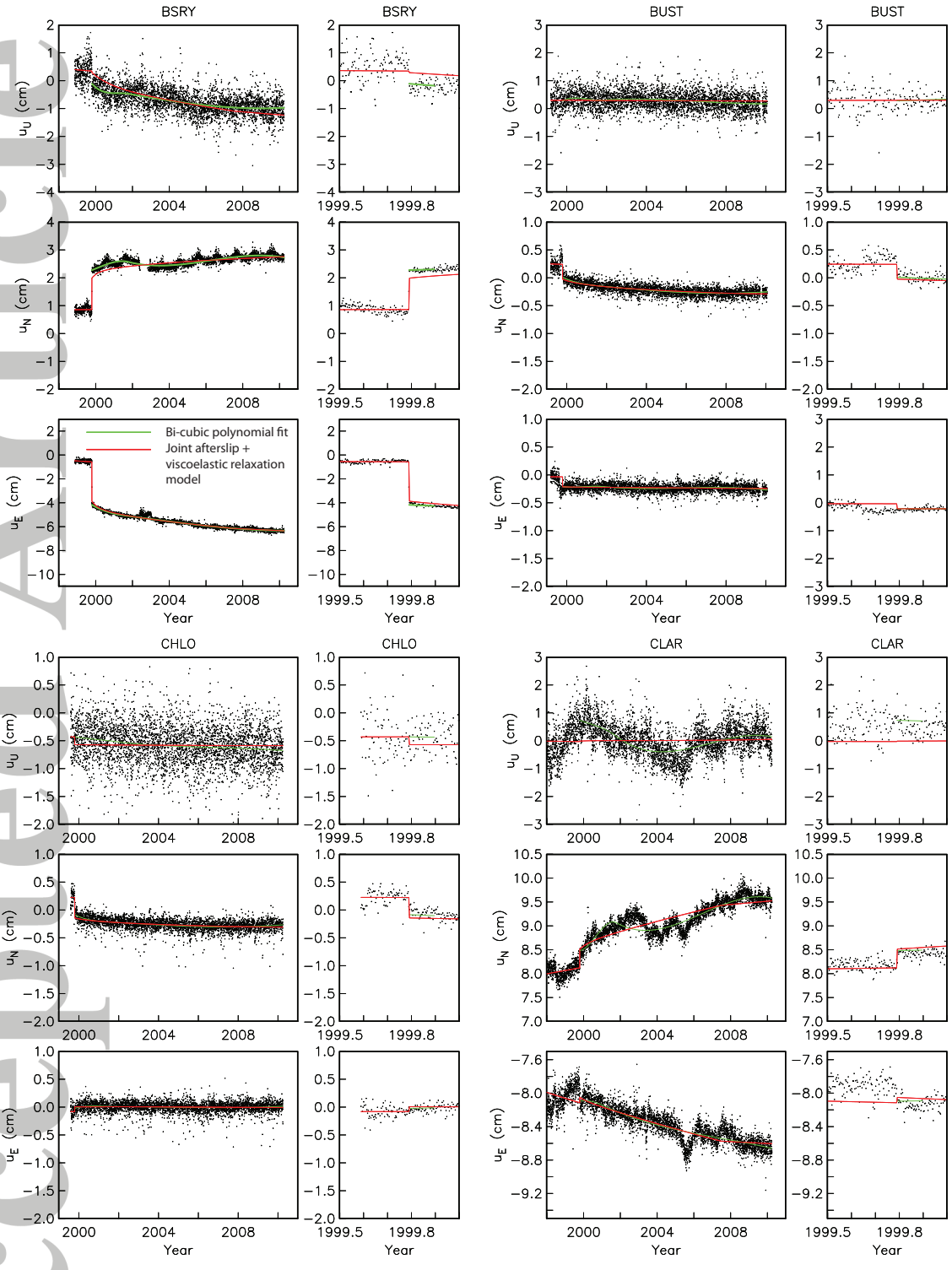

Figure 2. Time series of corrected observed displacement u'_{obs} (black dots) and corrected model displacement u'_{mod} (red curves) at selected stations (locations shown in Figure 1). Green curves are the bi-cubic polynomial fit to the post-Hector Mine portion of each time series. Model time series are on the optimal 2D viscoelastic structure (Figure 9) based on joint afterslip and viscoelastic relaxation modeling (section 5.3). u_E, u_N, and u_U refer to east, north, and up displacements, respectively.

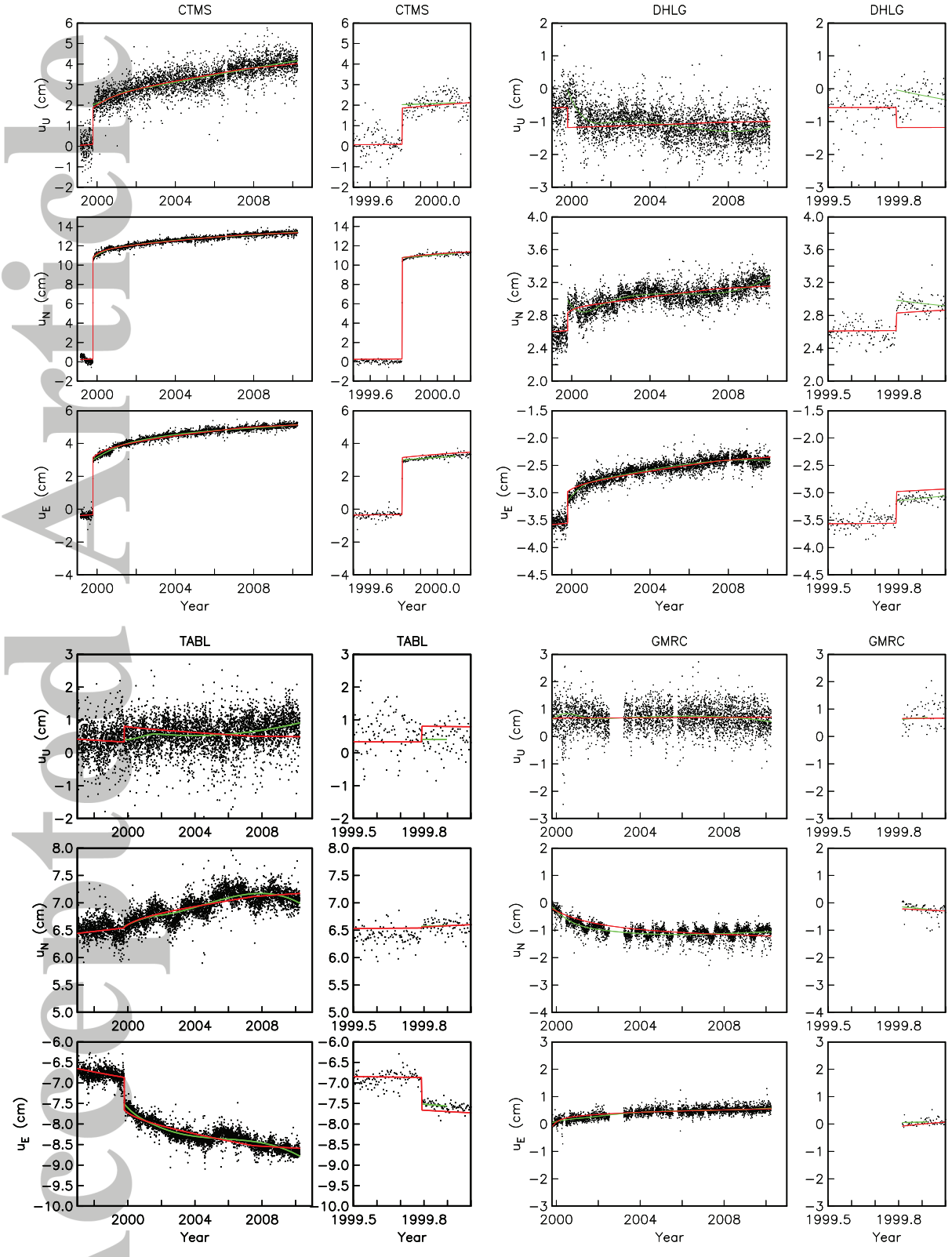

Figure 2. (continued)

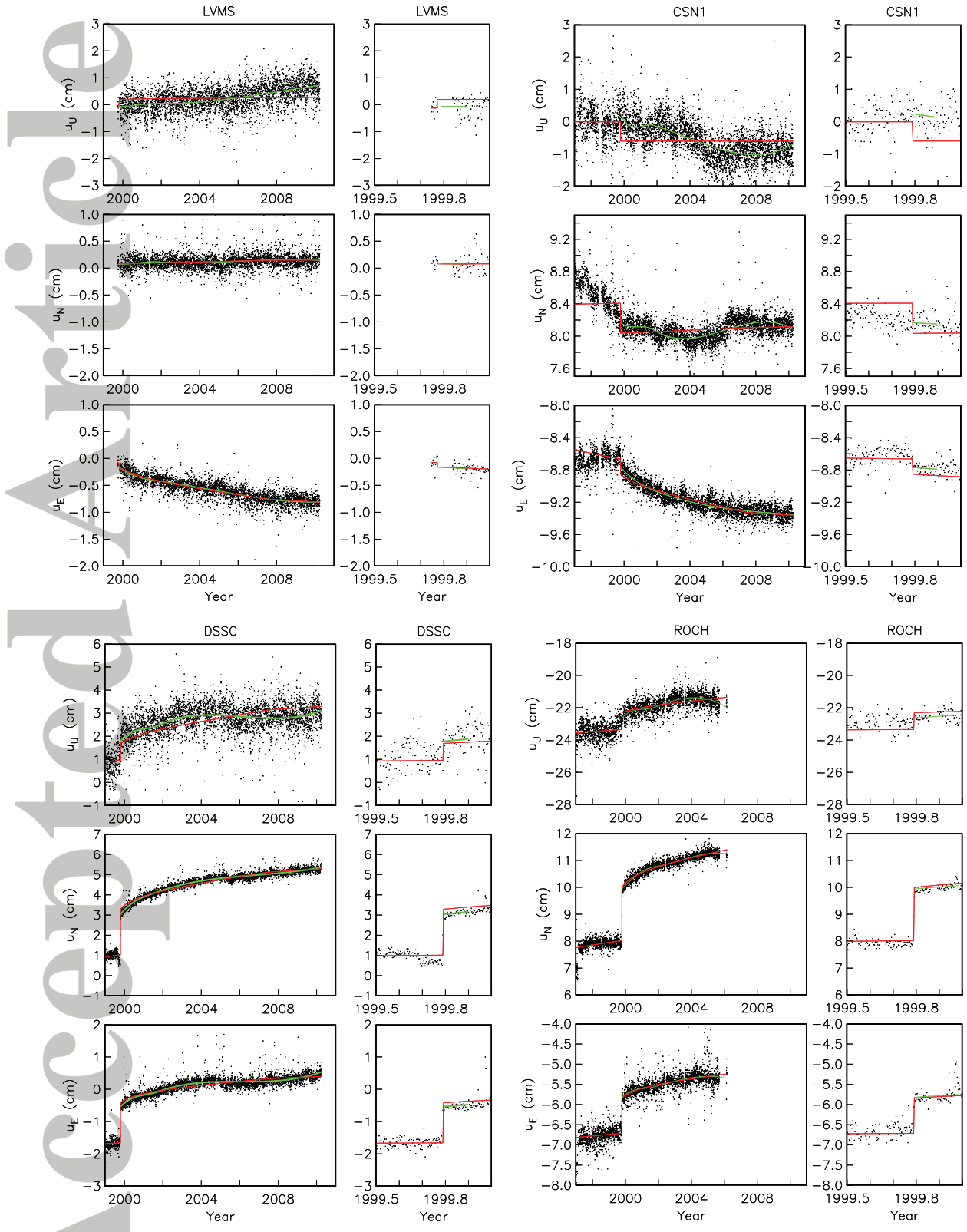

Figure 2. (continued)

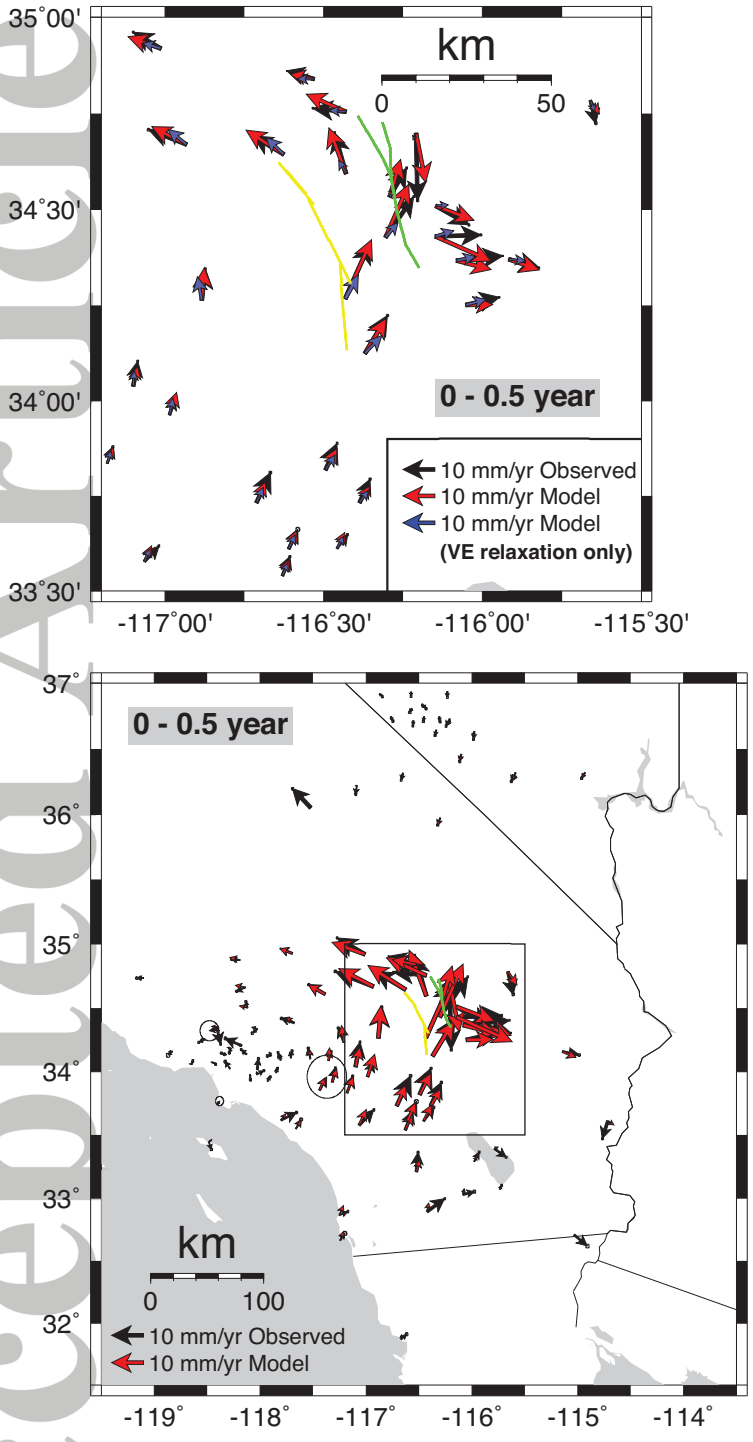

Figure 3. Observed transient velocity field u_{obs} (black vectors) and model transient velocity field u_{mod} (red vectors) in three distinct time periods. Model velocities are on the optimal 2D viscoelastic structure (Figure 9) based on joint afterslip and viscoelastic relaxation modeling (section 5.3).

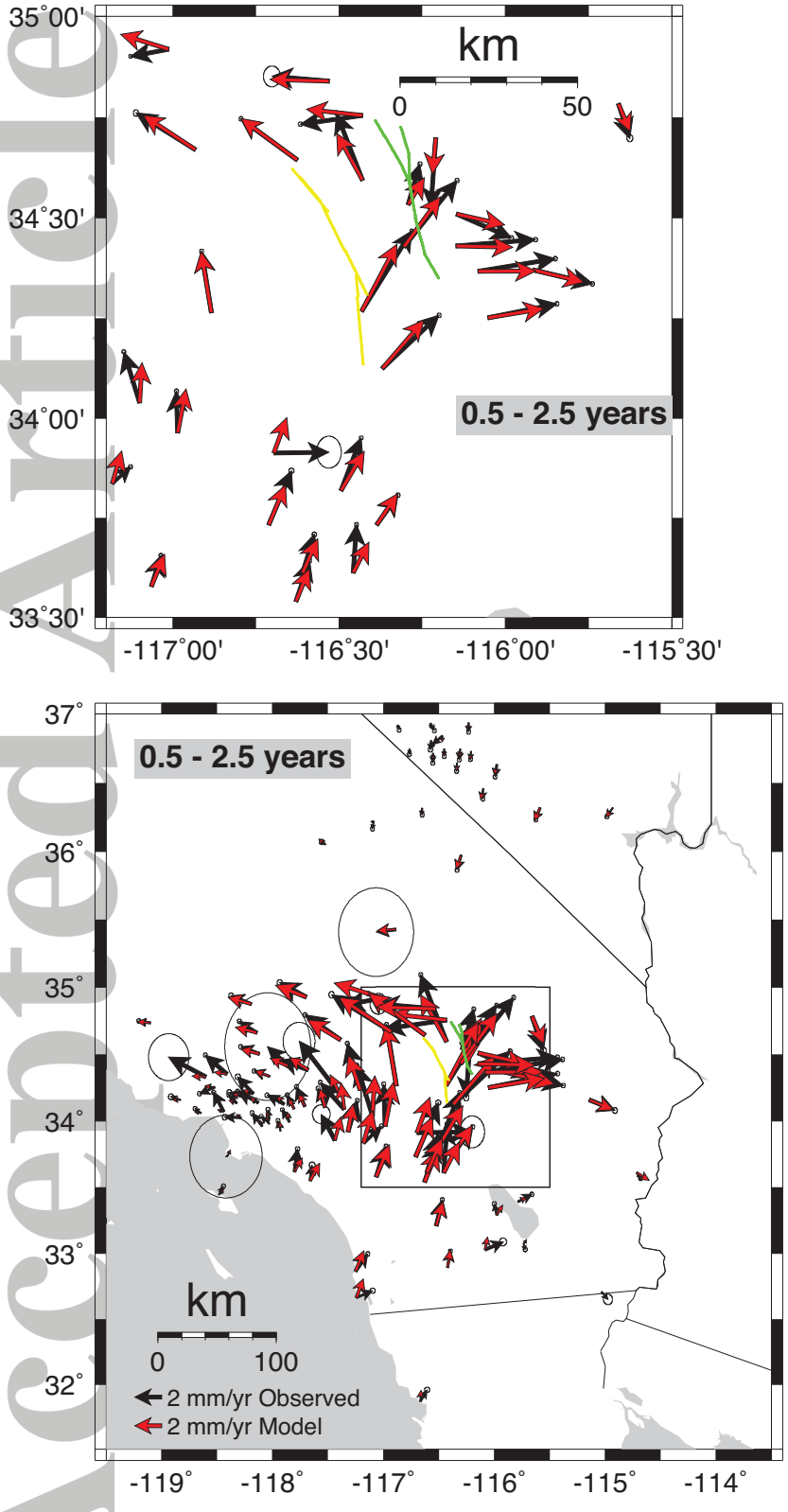

Figure 3. (continued)

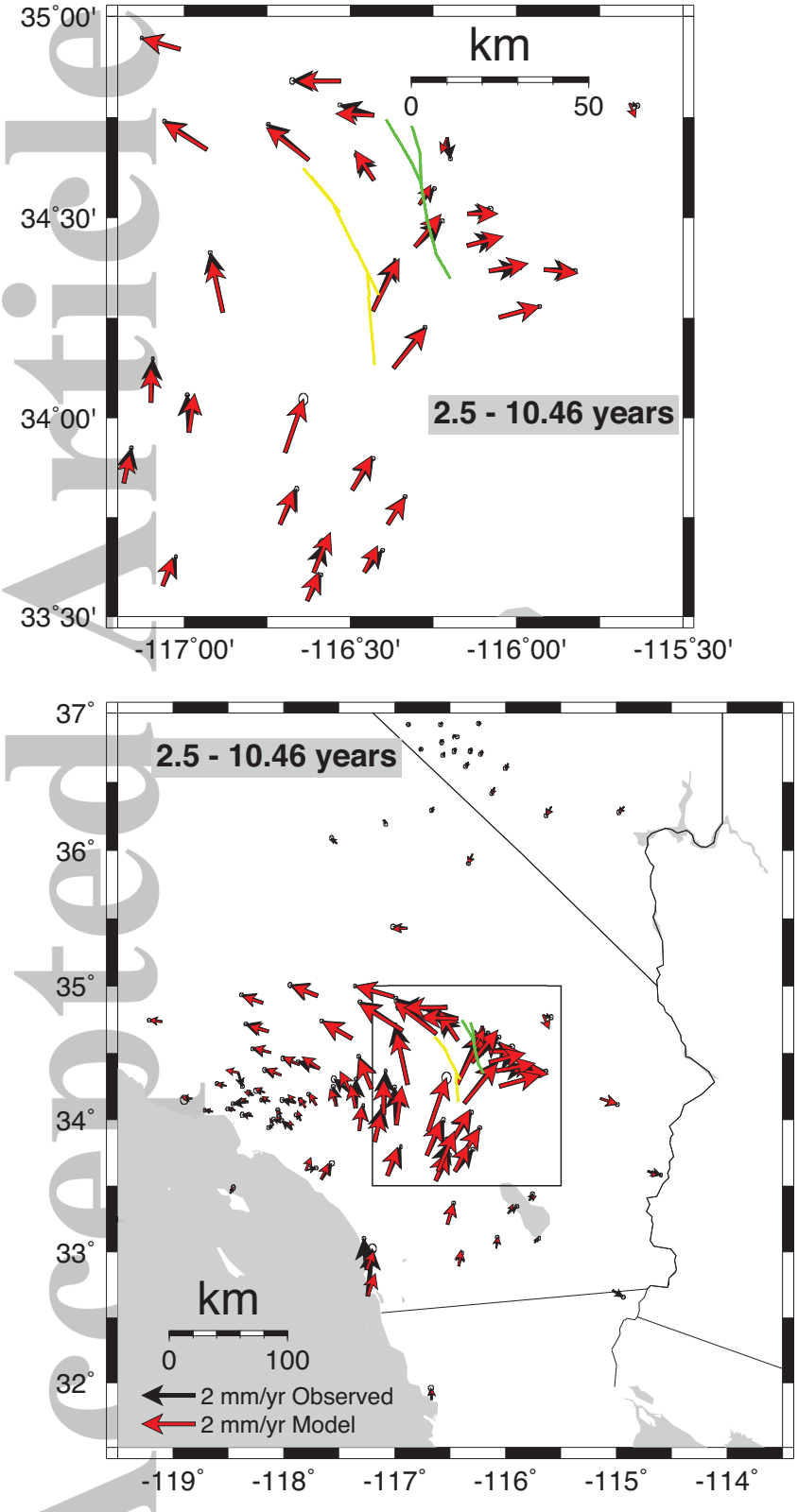

Figure 3. (continued)

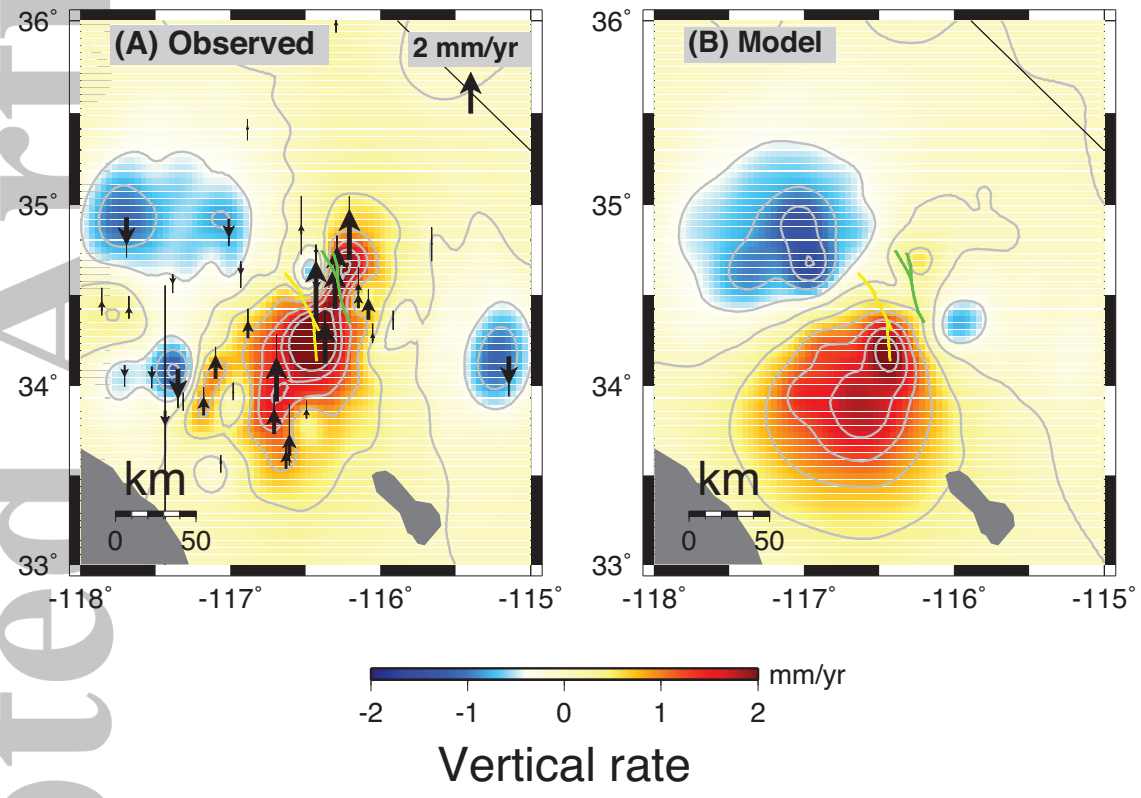

Figure 4. Smoothed observed and model vertical velocity u_{obs} and u_{mod}, respectively, from 0 to 10 years following the Hector Mine earthquake. To render them comparable with observations, model velocities are sampled only at contributing GPS sites before smoothing, and they are on the hybrid 2D viscoelastic structure (Figure 9) based on joint afterslip and viscoelastic relaxation modeling (section 5.3).

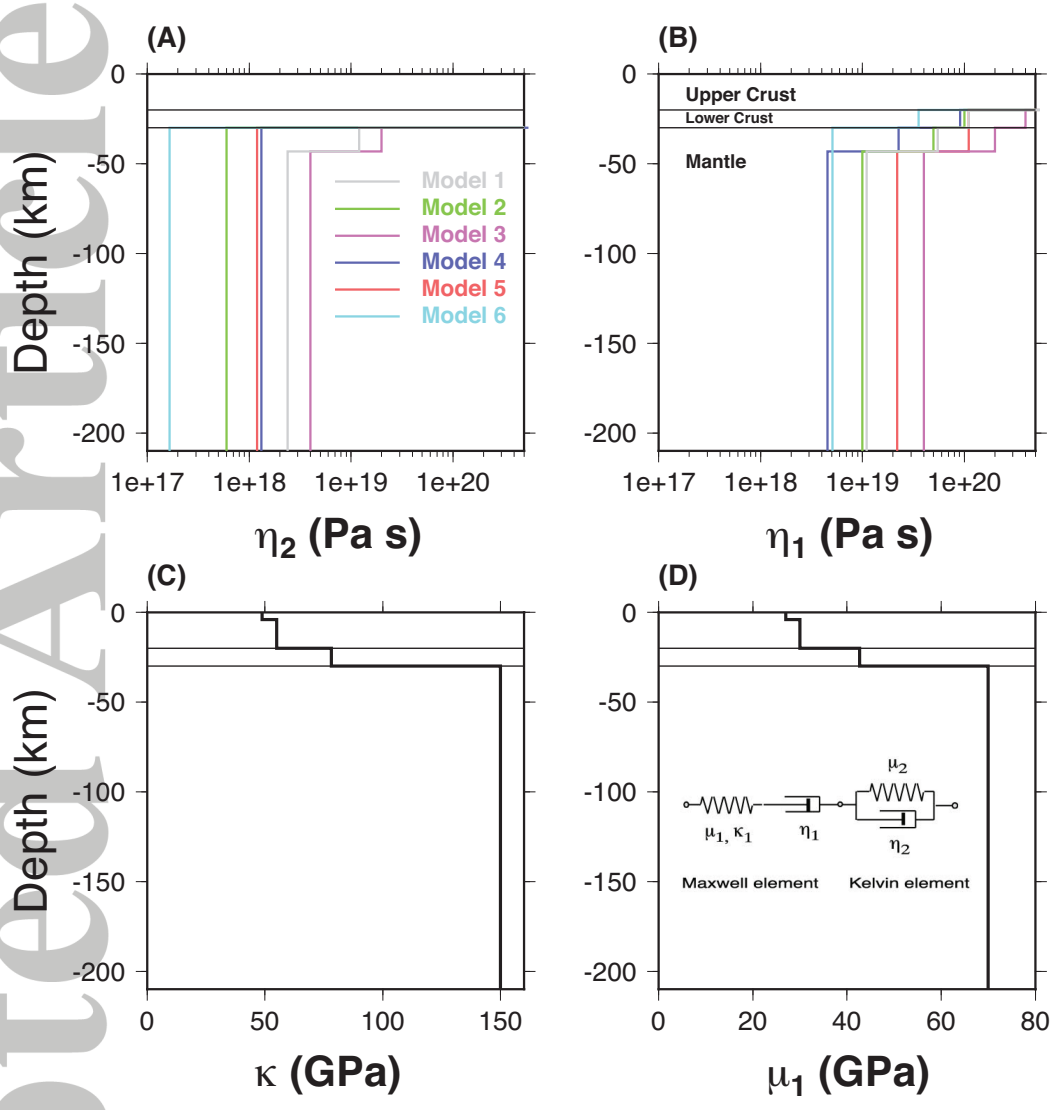

Figure 5. Laterally homogeneous Burgers body rheology models considered in this study. (a) and (b) show depth-dependent transient and steady state viscosity, respectively. (c) and (d) show the depth-dependent elastic bulk and shear modulus, respectively. All models have the same elastic structure (κ and μ_1) and the same transient shear modulus $\mu_2 = 70$ GPa in the mantle. The lower crust is assumed to be a Maxwell solid. The inset shows the components of the Burgers body, a Kelvin element with material relaxation time η_2/μ_2 in series with a Maxwell element with material relaxation time η_1/μ_1.

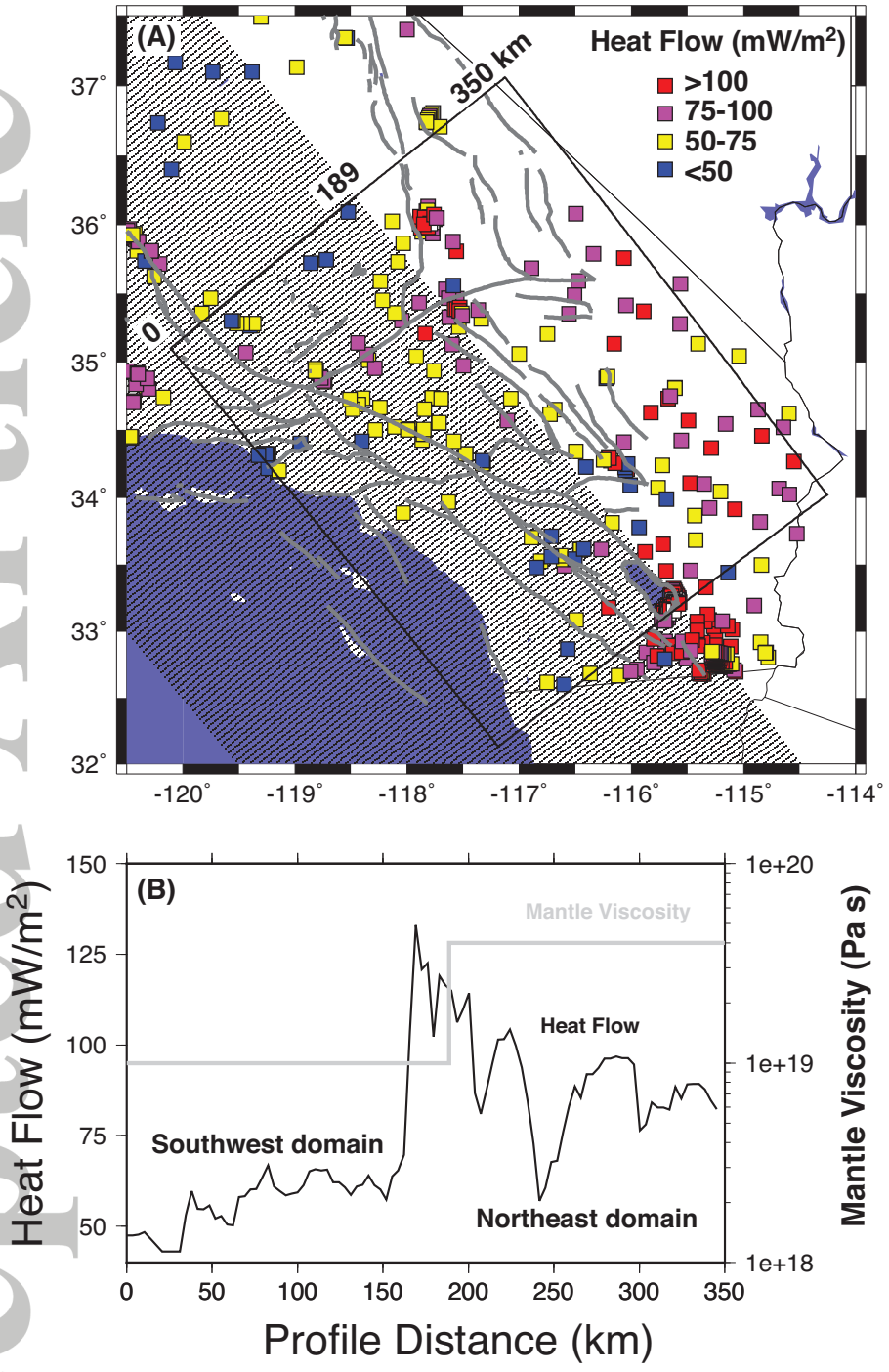

Figure 6. (a) Heat flow in southern California from the USGS online database. Southwest domain from Figure 1 is shaded. (b) Laterally averaged heat flow within the boxed region of (a) as a function of N50°E distance from the southwest edge of the box, using a 10 km averaging half-width along the profile. The steady-state mantle viscosity η_1 from the optimal 2D viscoelastic structure (Figure 9) is superimposed. Selected profile distances are labeled in (a).

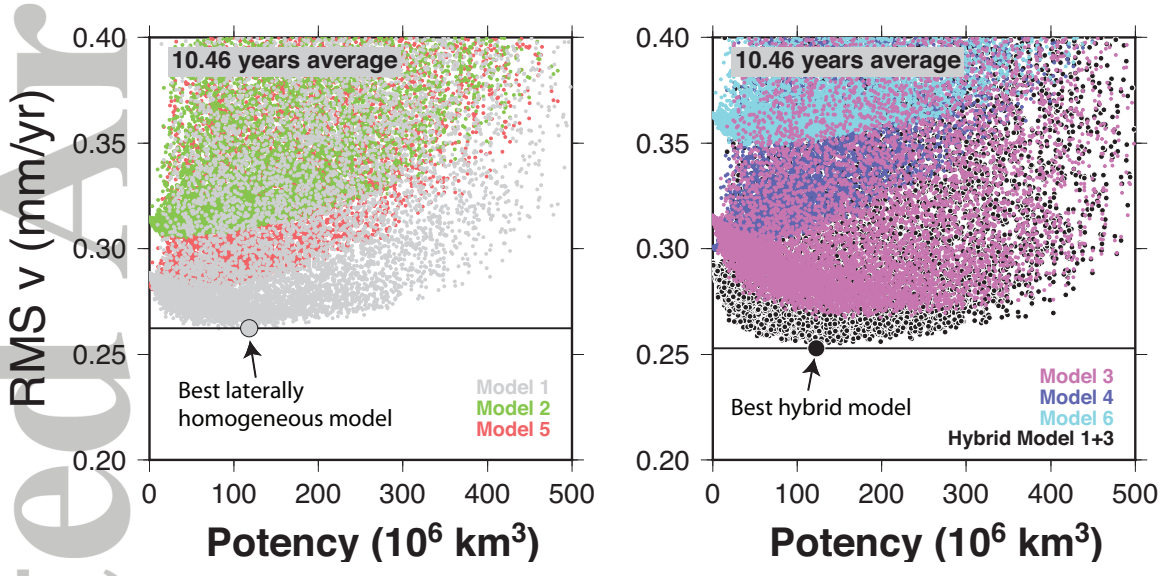

Figure 7. Model misfit RMS v averaged over all time periods for the six laterally homogeneous models prescribed in Figure 5, plus a hybrid 2D structure consisting of Model 3 structure in the northeast domain and Model 1 structure in the southwest domain (Figure 1), as a function of the potency of afterslip for 20000 illustrative (out of a total 200000) random afterslip models. The best-fitting laterally homogeneous and hybrid models are indicated with RMS v values of 0.262 and 0.252 mm/yr, respectively.

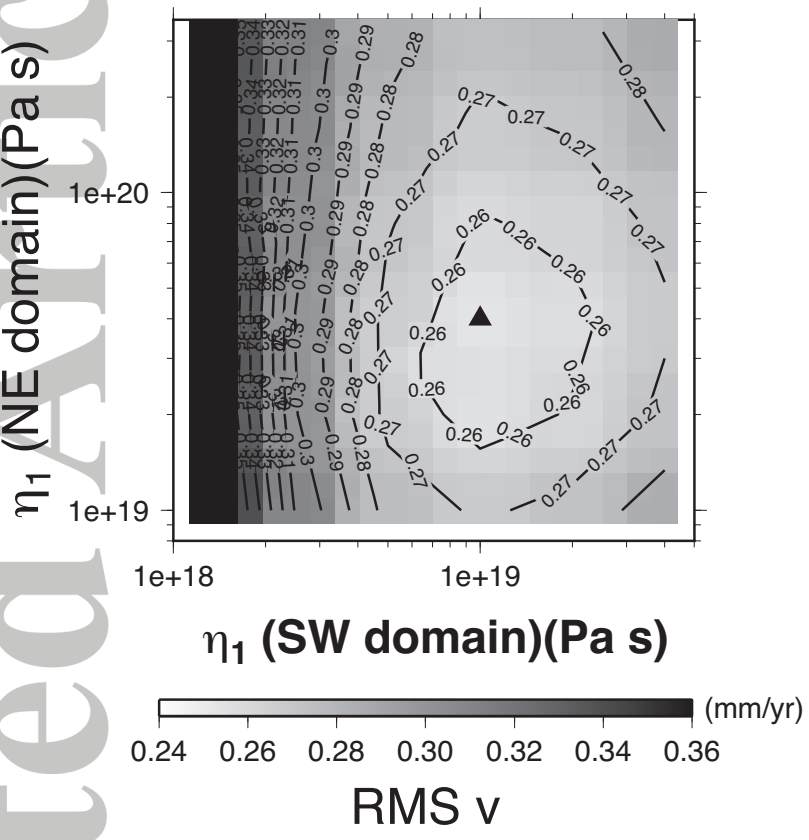

Figure 8. Overall misfit RMS v determined for a grid search of NE-domain and SW-domain steady-state mantle viscosities. The viscosity combination yielding the smallest misfit (optimal 2D viscoelastic structure) is indicated with the black triangle.

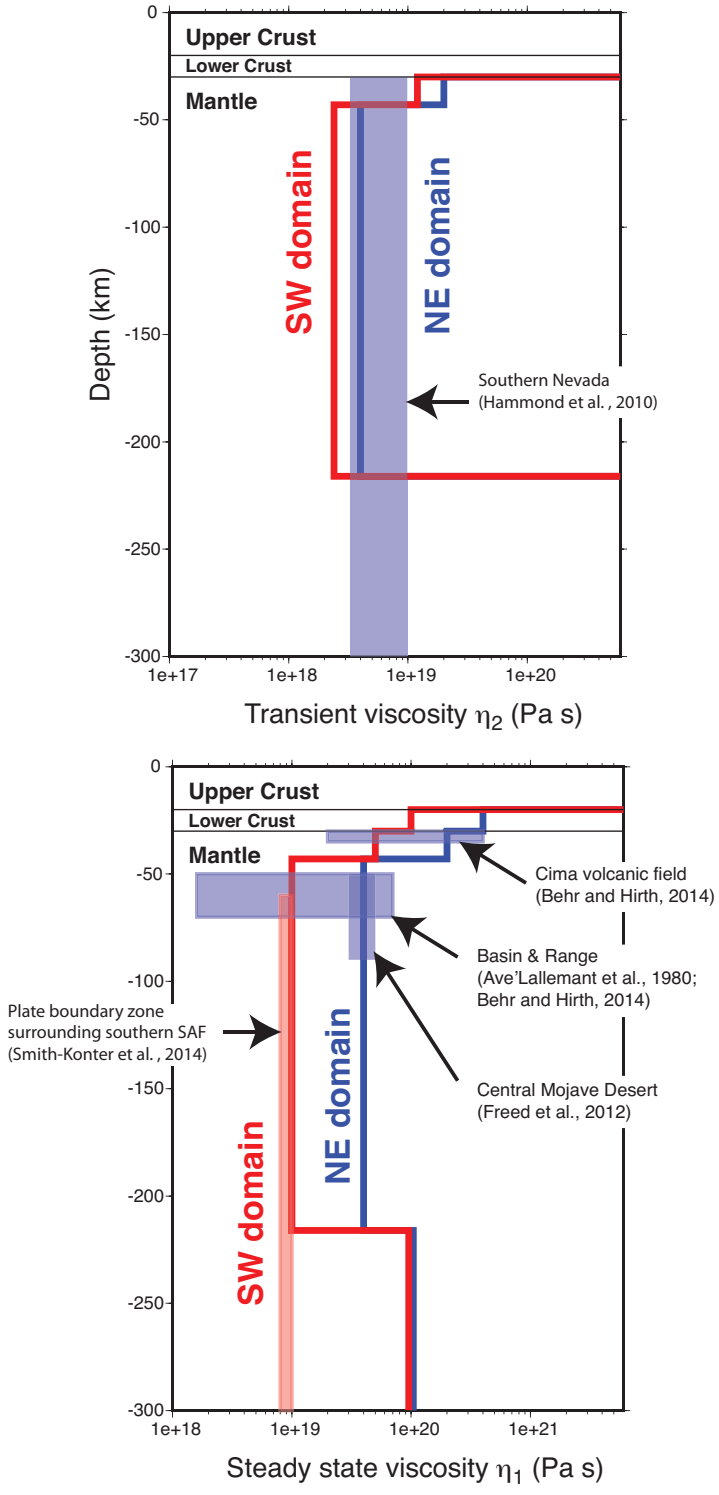

Figure 9. Optimal 2D Burgers body model determined in a grid search. (a) and (b) show depth-dependent transient and steady state viscosity, respectively, for the northeast and southwest structures represented by the black triangle in Figure 8. Both the northeast and southwest domains have the same elastic structure (Figure 5c,d) and the same transient shear modulus $\mu_2 = 70$ GPa in the mantle. The lower crust is assumed to be a Maxwell solid. Independent viscosity estimates for the appropriate region−− shaded as blue for the northeast domain and red for the southwest domain −− are shown as ranges in viscosity and depth according to the cited studies.

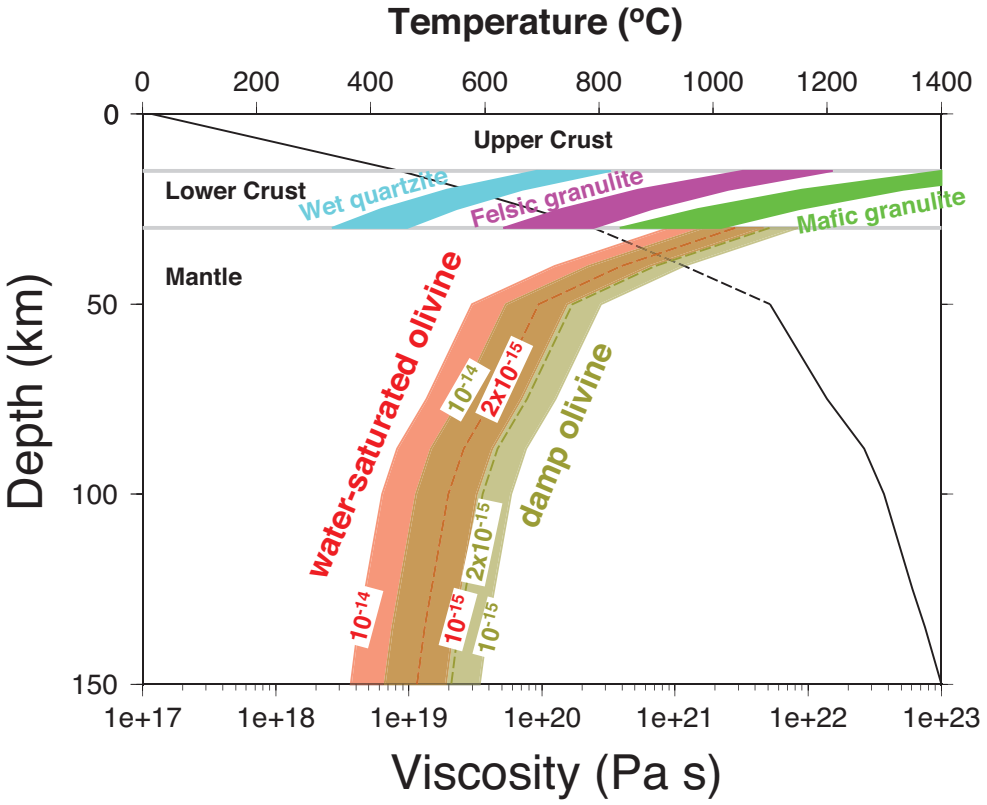

Figure 10. Steady-state viscosity as a function of depth for water-saturated and damp olivine in the mantle and lower crust materials at strain rates of 10^{-14}/s and 10^{-15}/s, and additionally at 2×10^{-15}/s in the mantle. Flow parameters for olivine aggregates are [*Hirth and Kohlstedt*, 2003] A=90 $(\mathrm{MPa})^{-(n+r)}$/s, $E^* = 480$ kJ/mol, $Q^* = 11 \times 10^{-6}\mathrm{m}^3$/mol, $n = 3.5$, and $r = 1.2$. Water concentration (C_{OH}) values for water-saturated olivine are provided by Table 3 of *Dixon et al.* [2004]; for 'damp' olivine C_{OH} is assigned 18% of the water-saturated values. In the mantle the temperature is the mean Western US geotherm of *Goes and van der Lee* [2002]. In the crust, the geotherm is prescribed by eqn (3) and Table 2 of *Afonso and Ranalli* [2004], with a surface heat flow of 70 $\mathrm{mW/m}^2$ and Moho depth of 30 km. Lower crust viscosity curves are based on material constants for wet quartzite [*Kirby and Kronenberg*, 1987], felsic granulite, and mafic granulite [*Wilks and Carter*, 1990].

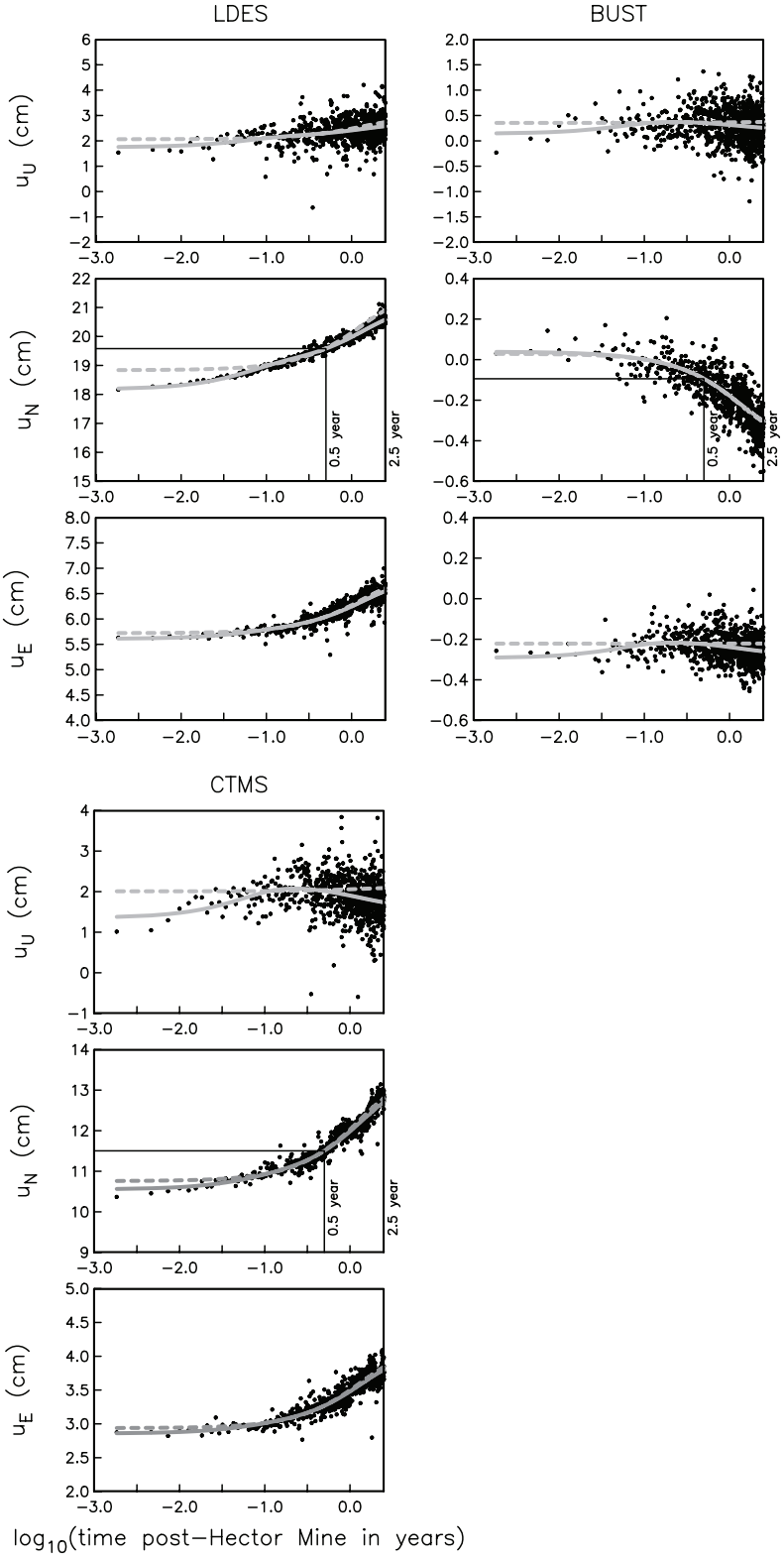

Figure 11. Observed time series at CTMS, LDES, and BUST are compared with the best-fitting curves of the form of eqn 18 (solid curves, $\tau_1 = 1.43$ year and $\tau_2 = 0.065$ year) or of the form of eqn 18 without the D term (dash curves, $\tau_1 = 1.43$ year). The cumulative postseismic displacement up to 0.5 years is indicated for each north-component time series (the north component dominates the relaxation at each site).

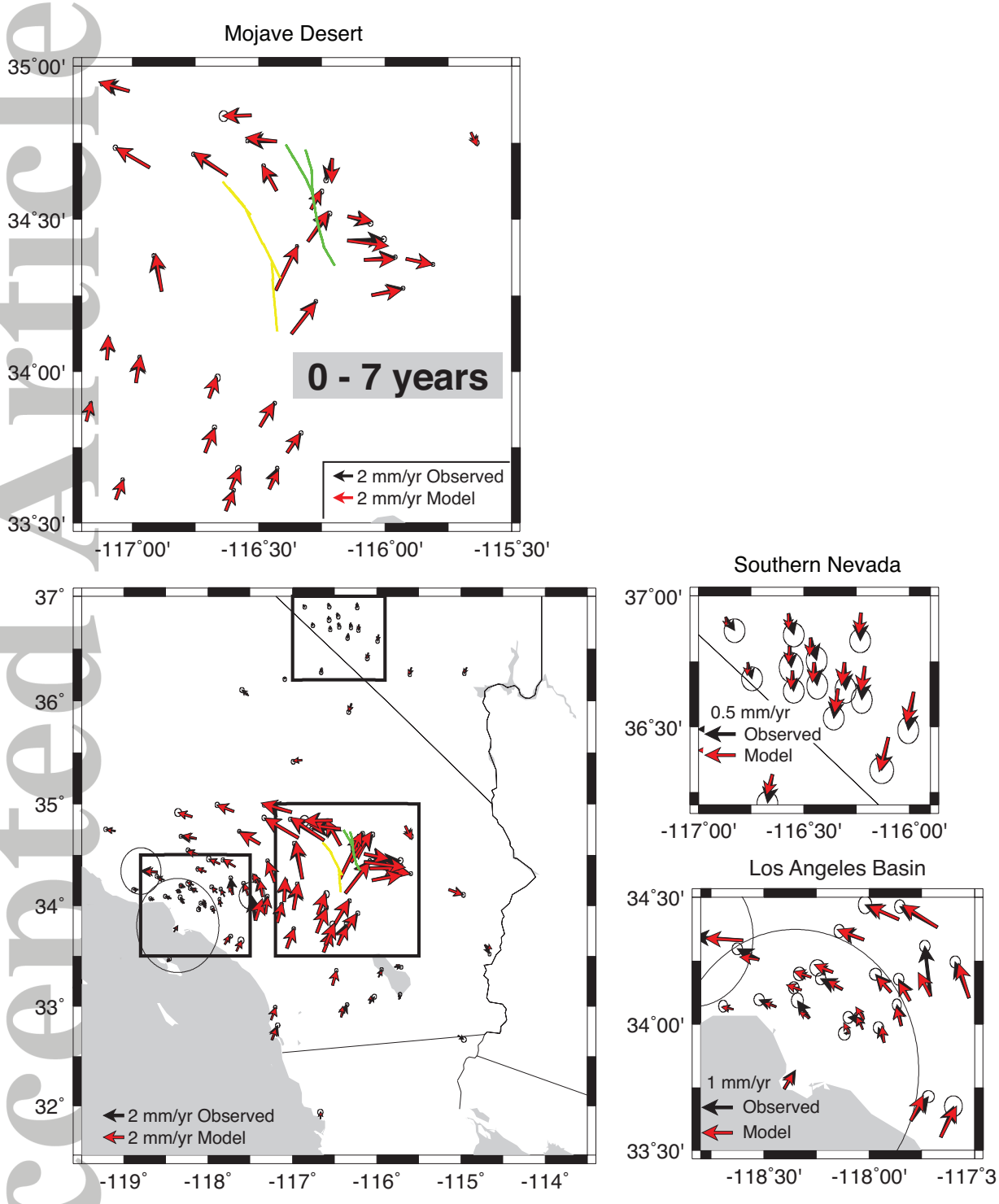

Figure 12. Observed transient velocity field (black vectors) and model transient velocity field (red vectors) in the 0 - 7 year time period. Model velocities are on the optimal 2D viscoelastic structure (Figure 9).

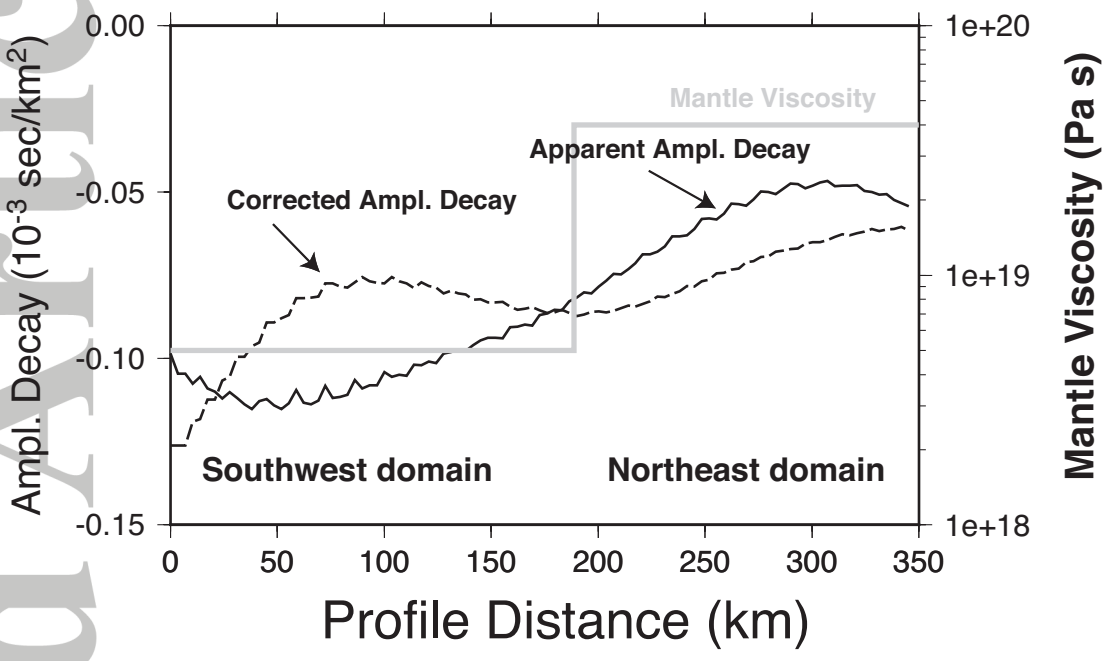

Figure 13. Laterally averaged amplitude decay of 60 sec Rayleigh waves (derived from Figure 11 of *Lin et al.* [2012]) within the boxed region of Figure 6a as a function of N50°E distance from the southwest edge of the box, using a 10 km averaging half-width along the profile. Separate curves are shown for apparent (solid curve) and corrected (dashed curve) amplitude decay. The steady-state mantle viscosity η_1 from the optimal 2D viscoelastic structure (Figure 9) is superimposed. Selected profile distances are labeled in Figure 6a. The generally larger amplitude decay and lower viscosity under the southwest domain are consistent with higher mantle water content under this domain.